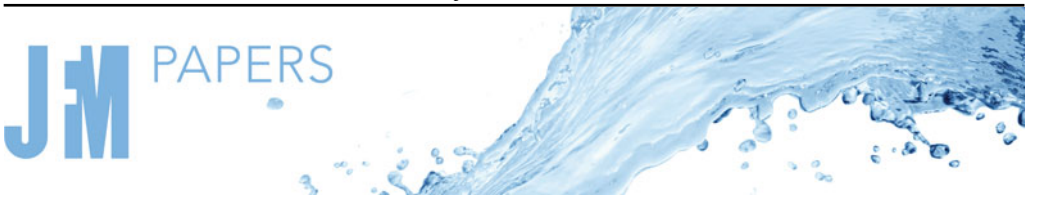
J. Fluid Mech. (2026), *vol.* 1037, A3, doi:10.1017/jfm.2026.11665



Effect of freestream turbulence on the coherent dynamics of a wind turbine wake

Neelakash Biswas[1] **and Oliver Buxton**[1]

[1]Department of Aeronautics, Imperial College London, London SW7 2AZ, UK

Corresponding author: Neelakash Biswas, biswasneelakash@gmail.com

(Received 26 June 2025 UTC; revised 18 March 2026 UTC; accepted 5 May 2026 UTC)

The wake of a model wind turbine exposed to incoming freestream turbulence (FST) with a variety of turbulent characteristics is studied through particle image velocimetry experiments. The FST cases were produced using different passive turbulence generating grids. The cases spanned turbulent intensities (T_i) in the range $1.3\,\% \lesssim T_i \lesssim 14\,\%$ and only considered short integral length scales $L_v \lesssim 0.2D$ (where D is the turbine diameter). Increasing T_i and L_v in this range resulted in an earlier breakdown of the tip vortices which is shown to be associated with increased wake meandering amplitudes. For all the FST cases considered, the initiation of wake meandering was found to be related to a turbine instability that is excited by the nacelle's shedding, even for the highest FST levels. The amplitudes of wake meandering were similar for all the cases in the near wake ($x < 2D$), but the amplitudes in the far wake ($x > 4D$) were discernibly higher for all the FST cases compared with the no grid case (lowest T_i), primarily due to the early break down of the tip vortices. Deeper insights into the origins, and subsequent evolution, of the various coherent motions (characterised by particular frequencies) in the presence of FST are obtained through analysis of the multiscale triple-decomposed coherent kinetic energy budgets. The wake meandering modes in the presence of FST are shown to better utilise the mean velocity shear, extracting more energy from the mean flow while other sources such as nonlinear triadic interactions and diffusion also become important.

Key words: vortex dynamics, vortex shedding, wakes

1. Introduction

Wind turbine wakes exhibit a large range of coherent structures such as the tip/root vortices, distinct vortex sheddings from the tower or the nacelle and wake meandering

© The Author(s), 2026. Published by Cambridge University Press. This is an Open Access article, distributed under the terms of the Creative Commons Attribution licence (https://creativecommons.org/licenses/by/4.0/), which permits unrestricted re-use, distribution and reproduction, provided the original article is properly cited.

https://doi.org/10.1017/jfm.2026.11665 Published online by Cambridge University Press

(Sherry *et al.* 2013; Okulov *et al.* 2014; De Cillis *et al.* 2021; Biswas and Buxton 2024*a*). These coherent structures play a critical role in determining the spatiotemporal evolution of the wake of a turbine (Lignarolo *et al.* 2015; Porté-Agel *et al.* 2020; Biswas and Buxton 2024*a*,*b*) and hence, can have large impacts on farm-level performance (Vermeer *et al.* 2003; Barthelmie *et al.* 2007; Sanderse *et al.* 2011; Stevens, & Meneveau 2017). The dynamics of the coherent structures depends on several factors including (i) the geometry of the turbine, such as the design of the blades (Abraham, & Leweke 2023; Dong *et al.* 2023); (ii) the operating conditions, such as the tip speed ratio λ, (defined as $\lambda = \Omega R/U_\infty$, where Ω is the turbine's rotational speed, R is the turbine radius and U_∞ is the freestream velocity) (Sherry *et al.* 2013; Okulov *et al.* 2014; Biswas and Buxton 2024*a*,*b*); (iii) freestream conditions such as the freestream turbulence (FST) level (Mao, & Sørensen 2018; Hodgson *et al.* 2023; Bourhis *et al.* 2025).

Real wind turbines are almost always exposed to some level of FST. The FST can be introduced for instance, due to the presence of the atmospheric boundary layer which is characterised by a broad range of scales due to the inherently large Reynolds number, or due to the presence of an upstream obstacle such as another wind turbine (Porté-Agel *et al.* 2020; Kosović *et al.* 2025). The nature and the level of turbulence in an atmospheric boundary layer is linked to the boundary layer characteristics such as the boundary layer thickness and atmospheric stability (Peña *et al.* 2016; Vahidi, & Porté-Agel 2024; Kosović *et al.* 2025). The level of FST is often measured using the turbulence intensity (T_i), defined as $T_i = \sqrt{(\overline{u'^2})}/U_\infty$ (where $\sqrt{(\overline{u'^2})}$ is the standard deviation of the velocity time history). In onshore sites wind turbines are exposed to higher T_i ($T_i < 15\,\%$) for most of their operating life (Elliott, & Cadogan 1990; Wagner *et al.* 2011; Peña *et al.* 2016), while for offshore sites freestream T_i is generally milder ($6\,\% < T_i < 8\,\%$) (Barthelmie *et al.* 2005; Türk, & Emeis 2010), due to the reduced surface roughness.

The effect of FST on the performance of a wind turbine is multifaceted. The FST can impart fluctuating loads (Eggers Jr *et al.* 2003; Robertson *et al.* 2019; Stanislawski *et al.* 2023; de Oliveira *et al.* 2025) and significantly alter the power output from a turbine (Maganga *et al.* 2010; Chamorro *et al.* 2013; Blackmore *et al.* 2016). Not only can it alter the performance of a standalone turbine, it can modify the spatiotemporal evolution of the wake, which can significantly change farm level performance (Porté-Agel *et al.* 2020). On one hand, FST can make the wake meander more in the lateral direction (Espana *et al.* 2012; Porté-Agel *et al.* 2020), potentially reaching other turbines in a staggered arrangement, imparting harmful unsteady loads (Larsen *et al.* 2008). On the other hand, FST can help re-energise the wake by enhancing lateral/vertical momentum transport from the freestream which can be beneficial for the downwind turbines in terms of power production (Gambuzza, & Ganapathisubramani 2023; Vahidi, & Porté-Agel 2024).

The effect of FST has been studied through a combination of numerical simulations (largely using large-eddy simulation), laboratory experiments using a small-scale representative wind turbine, and field experiments. High levels of FST have been shown to break down the tip vortices in the near wake (Chamorro, & Porté-Agel 2009; Wu, & Porté-Agel 2012). These vortices act as a 'shield' in the near wake, inhibiting the exchange of mass, momentum and kinetic energy (Medici 2005). Lignarolo *et al.* (2015) performed particle image velocimetry (PIV) experiments on a two-bladed wind turbine model and showed that there was a net kinetic energy entrainment into the wake only after the tip vortices broke down. Similar conclusions were reached for a three-bladed wind turbine (Eriksen, & Krogstad 2017; Biswas and Buxton 2024*b*). Therefore, high FST levels can accelerate wake recovery by breaking down this shield of vortices. In fact, a linear relationship between T_i and the wake recovery rate has been

https://doi.org/10.1017/jfm.2026.11665 Published online by Cambridge University Press

reported (Niayifar, & Porté-Agel 2016; Carbajo Fuertes *et al.* 2018; Gambuzza, & Ganapathisubramani 2023).

In the near wake, FST breaks down the dominant coherent structures, i.e. the tip vortices. In contrast, FST likely plays a different role on the dominant far wake structures, which have long been primarily associated with wake meandering. Although the dominance of wake meandering in the far wake has been known for many years, there still remain varied opinions on the genesis and characteristics of the meandering motion. For instance, a distinct wake meandering frequency has been reported when FST intensity was negligible (Okulov *et al.* 2014; Biswas and Buxton 2024*a*) thereby associating wake meandering to a rotor scale bluff body shedding type instability (Medici, & Alfredsson 2008; Howard *et al.* 2015). In contrast, in other works wake meandering has been treated as a 'random' unsteady oscillation of the far wake driven by FST (Porté-Agel *et al.* 2020). Here, the wind turbine wake was thought to be passively advected by the large-scale structures present in the FST (Larsen *et al.* 2008). However, later works suggested that wind turbines do not simply advect the structures present in the freestream, instead, a turbine has a dynamic response, i.e. certain frequencies in the freestream can be amplified in the wake (Chamorro *et al.* 2012; Singh *et al.* 2014; Mao, & Sørensen 2018; Heisel *et al.* 2018; Gupta, & Wan 2019; Hodgson *et al.* 2023), highlighting the importance of characterising the spectral content of the inflow. Chamorro *et al.* (2012) proposed that a turbine can be modelled as an 'active filter', generating or amplifying certain frequencies while dampening others. Similar results were obtained by Singh *et al.* (2014) who showed that the turbine made the velocity fluctuations in the wake more 'homogenised' compared with the incoming flow.

Mao & Sørensen (2018) identified nonlinear optimal perturbations to a wind turbine wake modelled as an actuator disk. They reported that as the inflow perturbation amplitude increased, the optimal perturbation frequency reduced from $St_{U_\infty,D} = 0.64$ to $St_{U_\infty,D} = 0.25$ (where $St_{U_\infty,D}$ denotes the Strouhal number based on the turbine diameter and freestream velocity) for $Re = 1000$ (based on turbine radius and freestream velocity). As Re was increased to 3000, the optimal perturbation frequency further reduced to $St_{U_\infty,D} = 0.16$. These low frequencies fall well within the accepted range of wake meandering frequencies (Medici, & Alfredsson 2008; Chamorro *et al.* 2013; Okulov *et al.* 2014). Beyond $Re = 3000$, Mao & Sørensen (2018) noted that the optimal frequency did not change, indicating a possible Re invariance at all application-specific Reynolds numbers. Similarly, the large-eddy simulation study of Foti, Yang & Sotiropoulos (2018) showed that the wake meandering amplitude, when properly scaled by the thrust, was largely invariant of the rotor size that spanned nearly three orders of magnitude (see figure 8*b* of Foti *et al.* (2018)). The authors, however, treated wake meandering as more of a bluff body shedding type instability of the turbine (Howard *et al.* 2015). Therefore, there is now a general consensus that in real wind turbines exposed to FST, the nature and intensity of wake meandering can depend on multiple factors including the turbine geometry, operating condition and FST (Howard *et al.* 2015; Mao, & Sørensen 2018; Gupta, & Wan 2019; Gambuzza, & Ganapathisubramani 2023; Dong *et al.* 2023; Biswas and Buxton 2024*a*; Wang *et al.* 2025). The relative importance of each of these factors is still not fully understood and can well differ in the near wake and the far wake of the turbine (Foti *et al.* 2018; Dong *et al.* 2023; Bourhis *et al.* 2025). Dong *et al.* (2023) studied three different blade designs under three different FST conditions but at similar thrust coefficient (C_T). Within three rotor diameters downstream of the turbine, the wake meandering amplitudes (measured using the standard deviation of the wake centreline) were similar for the different blade designs and turbulence levels. Farther downstream, however, the blade design producing the strongest hub vortex showed significantly stronger

https://doi.org/10.1017/jfm.2026.11665 Published online by Cambridge University Press

wake meandering. For all the blade designs, in the far wake, the high FST case showed slightly higher wake meandering compared with low/medium FST cases (see figure 19 of Dong *et al.* (2023)).

While the need to characterise the spectral content of the inflow has been realised for some time, the exact role of the freestream length/time scales on the dynamics of the wind turbine wake and the wake recovery process is still not fully understood. Larger freestream characteristic length scales were shown to induce a stronger wake meandering and were linked to a faster kinetic energy entrainment from the freestream towards the far wake (Blackmore *et al.* 2014; Vahidi, & Porté-Agel 2024). These studies, however, modelled the turbine as an actuator disk, hence the effect of the tip vortices in the near field was ignored. Interestingly, Hodgson *et al.* (2023) reported a shorter near wake region and faster wake recovery in wind turbines exposed to a flow with shorter integral time scales. The authors modelled the wind turbine using the actuator line method (i.e. the tip vortices were captured). Similarly, the PIV experiments by Gambuzza & Ganapathisubramani (2023) showed that for very large integral time scales in a non-Kolmogorov type flow (having a narrow-band contribution from the low frequencies), the wake recovered slowly compared with an inflow with a similar T_i but shorter integral time scale. The authors linked this observation to the delayed breakup of the tip shear layer for this type of flows. Interestingly, however, the recent experimental work by Bourhis *et al.* (2025) did not find any clear influence of the freestream integral length scales on the strength of the leading tip vortex frequencies. These results indicate that the effect of the freestream characteristic length scales on the near and far wake dynamics of a turbine and the wake recovery process is still far from clear.

In this work, we explore answers to some of these appealing questions by performing a series of time-resolved PIV experiments on a wind turbine model exposed to incoming FST having different turbulence intensities (T_i) and integral length scales (L_v). The wind turbine model included a nacelle and tower mimicking a real wind turbine. In particular, we attempt to better understand the following aspects. (i) How does the energy content at the dominant frequencies in the near-wake change with FST? (ii) In the absence of FST, Biswas and Buxton (2024*a*) found a scaling between the wake meandering frequency and λ indicating that wake meandering could be a rotor scale bluff body shedding type instability. How does the nature of wake meandering change in the presence of FST? (iii) How does FST affect the energy exchanges between the various coherent modes and how does it impact the wake recovery process? (iv) Finally, in all of the above what are the relative roles of T_i and L_v?

The paper is organised in the following way: in § 2 we present the details of the experimental campaigns undertaken to characterise the FST and to capture the wind-turbine wake. Section 3 thereafter discusses the important frequencies identified in the wake and how they interact with FST. The coherent modes associated with these frequencies are next discussed in § 4. Finally, we assess the energy exchange budgets of the coherent modes in § 5 followed by concluding remarks in the final section.

2. Methodology

Particle image velocimetry experiments were conducted in the hydrodynamics flume in the Department of Aeronautics at Imperial College London. The flume had a cross-sectional area of 60×60 cm^2 at the operating water depth. A schematic of the experimental set-up is shown in figure 1. The turbine diameter (D) was 0.2 m and the model was the same as that detailed in Biswas and Buxton (2024*a*,*b*). The blockage based on the turbine diameter was 8.7 % which is comparable to blockages encountered in previous

https://doi.org/10.1017/jfm.2026.11665 Published online by Cambridge University Press

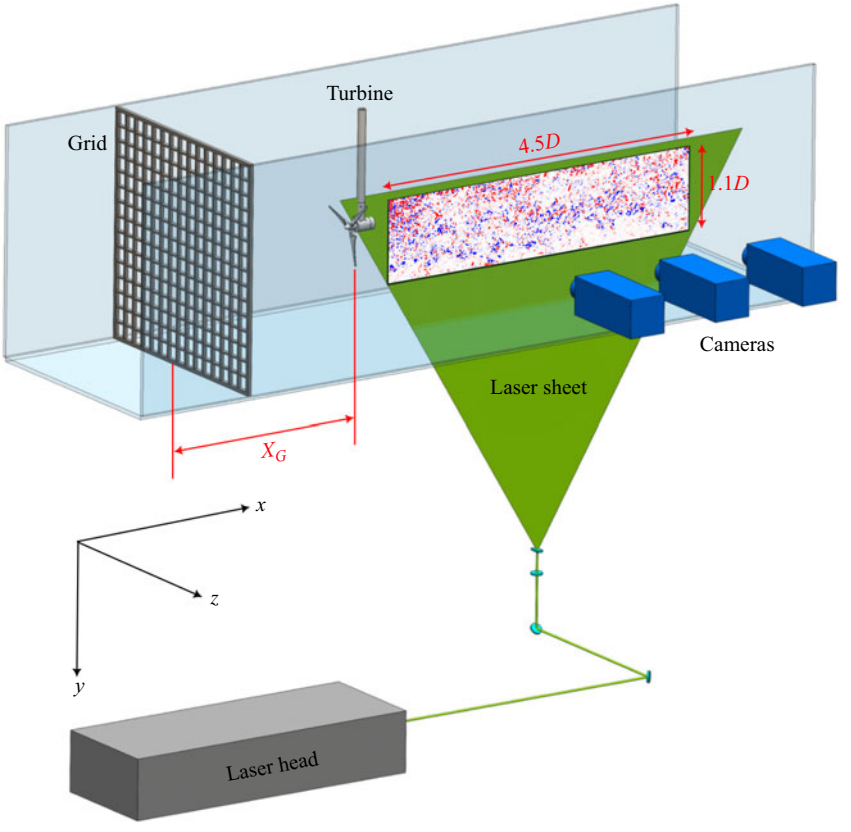


Figure 1. Schematic of the experimental set-up.

experimental studies (Sherry *et al.* 2013; Miller *et al.* 2019). The model had a nacelle (with diameter $D_{nac} = 0.033$ m) and tower (with diameter $D_T = 0.021$ m) associated with it such that it resembled a utility-scale turbine. The total blockage (rotor + tower) was 10 %. Note that in multimegawatt turbines, the nacelle diameter is often <5 % of the rotor diameter and the tower diameter is ≈ 3 % of the rotor diameter (Desmond *et al.* 2016). The design constraints in our experimental model, however, resulted in a nacelle diameter to rotor diameter ratio of 16.5 % and tower diameter to rotor diameter ratio of 10.5 %. Indeed in small-scale models used in laboratory experiments it has often not been possible to have a nacelle and tower with shape and size exactly similar to full-scale turbines (Chamorro *et al.* 2013; Howard *et al.* 2015; Barlas *et al.* 2016). The turbine was vertically hung into the flume in an inverted fashion as shown in figure 1. A stepper motor RS 829-3512 was used along with a drive and signal generator to rotate the turbine at a prescribed revolutions per minute. The motor, along with the speed controlling electronics, were located outside the flume and the torque from the motor was transmitted to the turbine shaft via a belt and pulley mechanism. The pulley and the shaft were placed inside the nacelle and the belt ran through the hollow tower which restricted any further reduction in the diameter of the nacelle or tower. The freestream velocity (U_∞) was kept constant at 0.2 m s^{-1}. Experiments were performed at a single tip speed ratio $\lambda_\infty = 6$ (defined as $\lambda = \Omega D/2U_\infty$, where Ω is the turbine's rotational speed). The Reynolds number based on the turbine diameter, Re_D was $\approx 40\,000$.

https://doi.org/10.1017/jfm.2026.11665 Published online by Cambridge University Press

The PIV experiments with the wind turbine had the same field of view (FOV) as that in experiment 1A discussed in Biswas and Buxton (2024*b*). Therefore, the details of the experiments are only briefly discussed here. Only planar PIV experiments were performed at the diametrical plane of the rotor aligned with the tower's axis. Three phantom v641 cameras were used to yield a stitched FOV spanning $\approx 4.5D$ in the streamwise (x) direction and $\approx 1.1D$ in the spanwise (y) direction. The origin of the coordinate system was placed at the rotor plane at the hub height. The experiments were time resolved. The acquisition frequency (100 Hz) was much higher than the turbine's rotational frequency (≈ 1.87 Hz). The spatial resolution of the experiments ($\approx 0.0115D$) was good enough to capture the tip vortices (having size $\approx 0.07D$). Data was obtained for a total time of 54.56 s (5457 snapshots) which corresponded to ≈ 102 rotor revolutions.

In previous experimental studies, different 'flavours' of FST, primarily characterised by different turbulence intensities (T_i) and freestream integral length scales (L_v), has been produced by either using a passive turbulence generating grid (Blackmore *et al.* 2016; de Oliveira *et al.* 2025) or using an active turbulence generating grid (Gambuzza, & Ganapathisubramani 2023; Bourhis *et al.* 2025). Active grids have been shown to be capable of producing turbulent Reynolds numbers and integral length scales much larger than those possible using passive grids (Kurian, & Fransson 2009; Hearst, & Lavoie 2015; Hearst *et al.* 2018). Despite limitations, passive grids have been extensively used in the literature primarily due to the ease of manufacturing and installation (Bearman, & Morel 1983; Fransson *et al.* 2005; Kankanwadi, & Buxton 2020). Using both types of grids, however, it is generally difficult to fill the top-left- and bottom-right-hand corners of a $T_i - L_v$ map, i.e. FST with very large integral length scales and very small turbulent intensities and *vice versa*.

In this work, we used four different passive turbulence generating grids to produce 10 different FST cases (including a reference case without a grid) similarly to our previous studies (Kankanwadi, & Buxton 2020; Chen, & Buxton 2023). Both regular and fractal grids were used (please see the Supplementary material for details are available at https://doi.org/10.1017/jfm.2026.11665). Two separate experimental campaigns were carried out to obtain the variation of T_i, L_v and the mean streamwise velocity ($\bar{U}$) behind the grids (without the turbine). The first experimental campaign used a single phantom v641 camera and had a thin strip like FOV of streamwise width $\approx 0.18D$, centred at a distance X_G from the grid, where the turbine would be placed (see figure 1). The values of X_G are tabulated in table 1. The transverse width of the FOV was $\approx 1.45D$, starting from close to the hub height of the turbine and reaching near the bottom wall of the flume. The profiles of T_i, L_v and $\bar{U}$ for all the cases studied (at a distance X_G from the grids) are shown in figures 2, 3 and 4, respectively. These experiments were also conducted at streamwise locations $X_G + 0.5D$ and $X_G + 4D$ in order to compare with data at the same locations in the presence of the turbine. In figures 2, 3 and 4, the blue and red dashed lines show the hub and tip heights, respectively. The profiles were averaged between these two lines and the rotor-averaged quantities are used to quantify the inflow. The parametric space (spanned by T_i and L_v) in this study is shown in figure 5(*a*) and the values are also tabulated in table 1. In figure 5(*a*), specific symbols are used for certain types of grids. The error bars show two standard deviations from the rotor averaged value within the rotor radius (see the transverse variations of T_i and L_v in figures 3 and 4) and hence mainly indicate the level of inhomogeneity in the inflow. The second experimental campaign simultaneously used two Phantom v641 cameras to give a stitched FOV of streamwise width $\approx 2.45D$ (49 cm) and transverse width $\approx 0.9D$ (18 cm). The grid was moved upstream keeping the optical set-up intact and a number of non-synchronous experiments were conducted for a particular grid to obtain time averaged statistics over a

https://doi.org/10.1017/jfm.2026.11665 Published online by Cambridge University Press

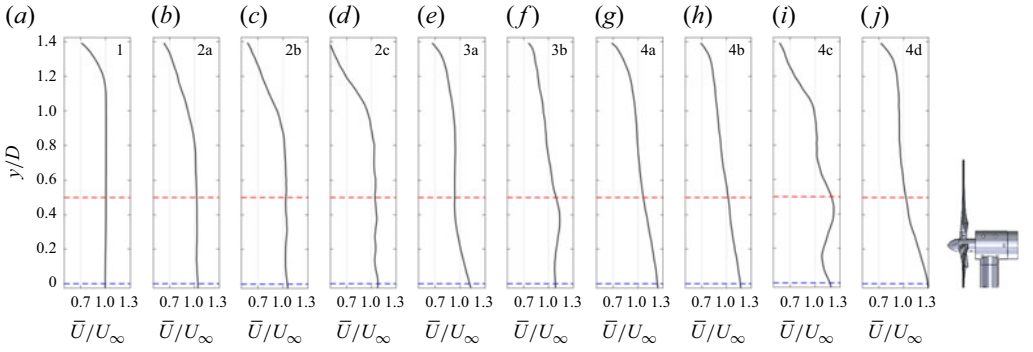


Figure 2. Profiles of mean streamwise velocity at the rotor plane (with the turbine removed). The cases are shown on the top right-hand corner. The tip and the hub heights are shown by the red and blue dashed lines, respectively.

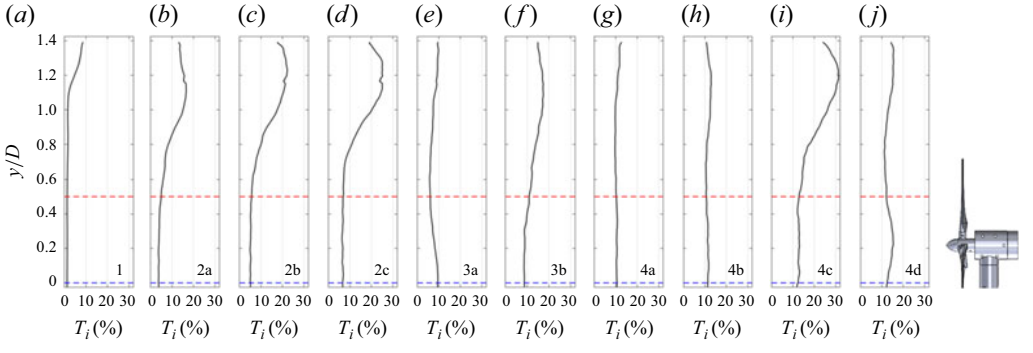


Figure 3. Turbulent intensity profiles at the rotor plane (with the turbine removed). The cases are shown on the bottom right-hand corner.

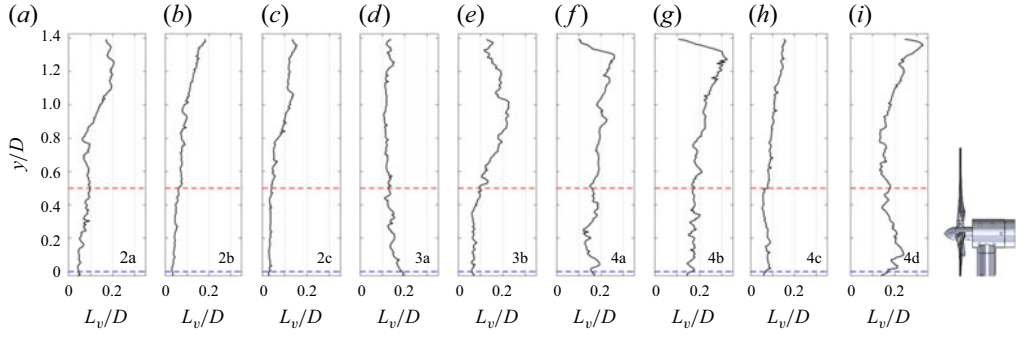


Figure 4. Profiles of integral length scales at the rotor plane (with the turbine removed). The cases are shown on the bottom right-hand corner.

certain streamwise distance as required. The results from the second campaign are only included in the Supplementary material.

In table 1, the distance between the grid and the turbine (X_G) is also shown in terms mesh size (M) for the regular grids and the wake intersection length scale (x^*) for the fractal grids. Here x^* is defined as $x^* = L_0^2/t_0$, where L_0 and t_0 represent the

https://doi.org/10.1017/jfm.2026.11665 Published online by Cambridge University Press

Case	Grid	X_G	T_i (%)	L_v (D)	U_b/U_∞	λ_{eff}
1	—	—	1.32 ± 0.06	$\leqslant 0.025$	1.0 ± 0.01	6.0
2a	SRG38	$5D(26.6M)$	4.04 ± 0.63	0.068 ± 0.035	1.03 ± 0.01	5.82 ± 0.04
2b	SRG38	$3.5D$ $(18.6M)$	5.18 ± 0.30	0.046 ± 0.016	1.04 ± 0.01	5.78 ± 0.07
2c	SRG38	$2.5D$ $(13.3M)$	6.64 ± 0.31	0.035 ± 0.007	1.05 ± 0.02	5.68 ± 0.11
3a	SFG5	$15D$ $(0.47x^*)$	7.74 ± 2.53	0.143 ± 0.033	1.0 ± 0.11	6.01 ± 0.68
3b	SRG111	$6D$ $(10.8M)$	9.26 ± 1.57	0.070 ± 0.014	1.10 ± 0.05	5.43 ± 0.22
4a	SFG7	$17D$ $(0.58x^*)$	10.53 ± 0.25	0.164 ± 0.052	1.15 ± 0.10	5.2 ± 0.46
4b	SFG7	$15D$ $(0.51x^*)$	11.29 ± 0.64	0.172 ± 0.021	1.09 ± 0.09	5.51 ± 0.46
4c	SRG111	$3.5D$ $(6.3M)$	12.70 ± 0.50	0.070 ± 0.022	1.15 ± 0.10	5.2 ± 0.45
4d	SFG7	$10D$ $(0.34x^*)$	13.96 ± 2.0	0.189 ± 0.052	1.15 ± 0.17	5.21 ± 0.77

Table 1. Parameters associated with the different experiments. Here X_G denotes the distance between the grid and the turbine, x^* is the wake intersection length scale for the fractal grids (Mazellier & Vassilicos 2010), M is the mesh size of the regular grids, U_b denotes the rotor averaged bulk velocity, λ_{eff} is the tip speed ratio based on U_b.

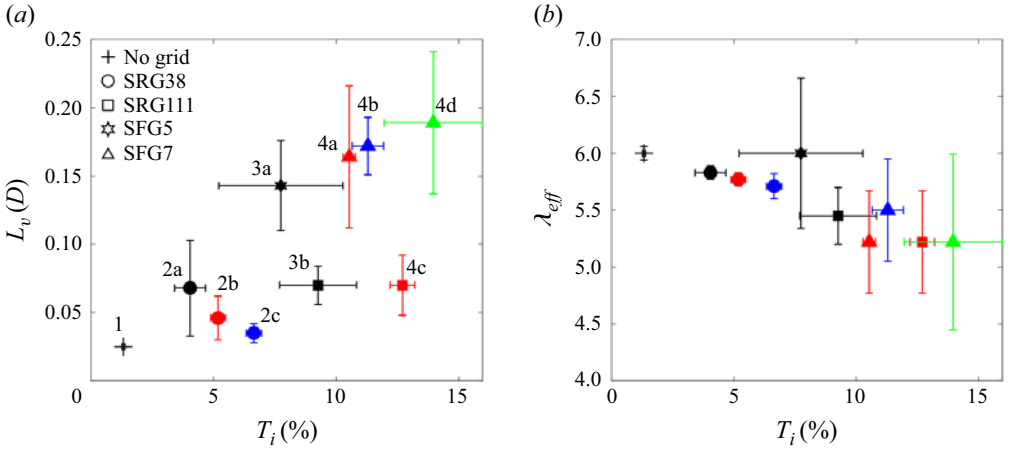


Figure 5. (*a*) Parameter space of turbulence intensity (T_i) and integral length scale (L_v) produced by different turbulence generating grids. The symbols show the values averaged over the rotor radius. Panel (*b*) shows the effective tip speed ratios (λ_{eff}) for $\lambda_\infty = 6$. Here λ_{eff} is measured based on the rotor averaged bulk velocity, U_b instead of U_∞ and hence is lower than λ_∞. The same symbol is used for a particular type of grid used as indicated in (*a*). The cases are also indicated in (*a*).

length and thickness of the largest bars of the fractal grids (Mazellier, & Vassilicos 2010; Kankanwadi, & Buxton 2020). For the regular grids there is a monotonic decay of turbulence and the turbulence becomes more homogeneous with downstream distance from the grid. For the fractal grids on the other hand, turbulence develops more slowly. For the latter, T_i generally peaks around $x = 0.45x^*$ and the flow starts to become homogeneous at around $x = 0.5x^*$ (Mazellier, & Vassilicos 2010). Considering several additional experimental constraints, however, the grids had to be placed at locations with respect to the turbine where the inflow turbulence is not homogeneous, especially for the highest FST cases. Additionally for some of the cases, especially cases 2c and 4c (closer to the regular grids) T_i, L_v and $\bar{U}$ also had a considerable streamwise gradient. The streamwise variation of T_i, L_v and $\bar{U}$ behind all the turbulence generating grids is shown

https://doi.org/10.1017/jfm.2026.11665 Published online by Cambridge University Press

in the Supplementary material. Nevertheless, the inhomogeneity of the inflow turbulence likely only has a secondary role on the dynamics of the wake as we will be discussing.

One of the other factors that had to be considered while positioning the grid was the interaction of the grid with the boundary layer developing at the bottom surface of the flume. For instance, the regular grid SRG38 was found to strongly interact with the boundary layer. This was most likely because this grid had horizontal bars closest to the bottom wall of the flume (highest local blockage) in the central laser plane (see figure 1 in the Supplementary material). It can be seen from figure 2, how the boundary layer gets progressively thicker as we move downstream of the grid (from figure 2*d* to figure 2*b*). Therefore, farther away from the grid, although we could gain in terms of homogeneity, the boundary layer would introduce unwanted additional turbulence. For the case 2a, although the turbine was placed outside the boundary layer at the rotor plane, farther downstream ($x > 3D$), the turbine wake intersected the boundary layer. Therefore, for this particular case, the results were only discussed up to $x/D = 3$. This was less of an issue for the other grids. The regular grid SRG111 was intentionally placed closer to the turbine to create the cases 3b and 4c with relatively higher T_i but at the expense of homogeneity. For the fractal grids on the other hand, since the turbulence develops much more slowly, a much higher X_G was necessary. Now, the turbine had to be placed towards the upstream end of the test section in order to have a large portion of the wake captured in the test section measurement area (see figure 1). This resulted in the distance between the turbine and the upstream end of the flume being limited to ≈ 3 m ($15D$). So the highest X_G tested without shortening the streamwise extent of the wake measured was $15D$. Only for case 4a, the fractal grid SFG7 was placed at $X_G = 17D$, but with the wake measured up to $x/D = 3$ to see if there is a significant change in the near wake dynamics.

Estimating integral length scales involves inherent intricacies and different methods can yield non-identical results. For instance, the integral length scales can be obtained by using the power spectra, by direct computation of the spatial autocorrelation function or by obtaining integral time scales using the temporal autocorrelation and then invoking Taylor's hypothesis of frozen turbulence. In this work, we use the spatial autocorrelation function. The integral length scales are estimated as $L_v = \int_0^{\hat{r}} R'_{12} dr$, where R'_{12} is the transverse autocorrelation function of the streamwise velocity fluctuations. R'_{12} is obtained using the following equation:

$$R'_{12}(\boldsymbol{x}, \boldsymbol{y}, r) = \frac{\overline{u'_1(\boldsymbol{x}, \boldsymbol{y}) u'_1(\boldsymbol{x}, \boldsymbol{y} + r\boldsymbol{e}_2)}}{\sqrt{\overline{u'_1(\boldsymbol{x}, \boldsymbol{y})^2}} \sqrt{\overline{u'_1(\boldsymbol{x}, \boldsymbol{y} + r\boldsymbol{e}_2)^2}}}. \tag{2.1}$$

Here the overbars denote averaging over time. Here u'_1 is the streamwise velocity fluctuation and $r\boldsymbol{e}_2$ represents some displacement r along the $\boldsymbol{e}_2$ direction ($\boldsymbol{e}_2$ is the unit vector along the spanwise, y direction). Finally L_v is calculated by integrating R'_{12} up to a certain distance $\hat{r}$ where R'_{12} first becomes zero. Further details about the quantification of the integral length scales and the sources of uncertainties have been added in Appendix A and in the Supplementary material. It is worthwhile mentioning that other transverse or streamwise autocorrelation functions were also tested. It was seen that the streamwise autocorrelation function of the transverse velocity (R'_{21}) yielded integral length scales of magnitude similar to that obtained using R'_{12} whilst, the streamwise autocorrelation function of the streamwise velocity (R'_{11}) yielded larger (up to 2−3 times) integral length scales. However, the autocorrelation functions R'_{12} or R'_{21} more often fell off to zero compared with R'_{11} which exhibited long range correlations. Therefore, only the integral length scales calculated using R'_{12} are discussed here. A more detailed discussion on

https://doi.org/10.1017/jfm.2026.11665 Published online by Cambridge University Press

the different correlations can be found in the Supplementary material. Nevertheless, the largest integral length scales we are able to produce here ($< 0.2D$ using R'_{12} or $< 0.45D$ using R'_{11}) are an order of magnitude smaller than the largest length scales a real wind turbine residing in an atmospheric boundary layer can be exposed to (Larsen *et al.* 2007; Porté-Agel *et al.* 2020). The current study is thus only able to explore the effect of short FST length scales on the near wake dynamics of a turbine.

The grids also introduce a blockage to the freestream, resulting in an acceleration of the incoming flow (please see the Supplementary material). Although the tip speed ratio based on U_∞ (denoted as λ_∞) was kept constant at 6 for all the FST cases, due to the blockage induced increment of the freestream velocity (see figure 2), the effective tip speed ratio (defined as $\lambda_{eff} = \lambda_\infty U_\infty / U_b$) reduced for all the FST cases. Here U_b is the rotor averaged bulk velocity. λ_{eff} for the different cases is shown in figure 5(*b*). The uncertainties are due to the transverse variation of the mean streamwise velocity as shown in figure 2. The variation of the power (C_P) and thrust coefficients (C_T) as a function of the tip speed ratio were obtained in our previous work using the blade element momentum method (Biswas and Buxton 2024*a*) (please see figure 15*b*). For the range of λ_{eff} observed here, the variation in the C_P and C_T was expected to be marginal. The test cases are divided into four subgroups, primarily based on turbulence intensity. Group 1 has negligible T_i while groups 2, 3 and 4 have low, mild and high T_i, respectively. Nevertheless, hard boundaries likely do not exist between the adjacent subgroups.

3. Effect of FST on the dynamics of the wake

Instantaneous vorticity fields for six cases, case 1 (no grid case), 2a, 2c, 3b, 4b and 4d are shown in figure 6 for $\lambda_\infty = 6$ (see also Supplementary movies 1–6). These cases represent the wake at increasing turbulence intensities. The instantaneous vorticity fields show a rich variety of scales present in the flow. The individual tip vortices and the merged vortices are the most clearly observed for the no grid case (case 1) as highlighted in figure 6(*a*). Here, the tip vortices undergo merging at $x/D \approx 1.5$ similarly to the observation in our earlier study through a different set of experiments (Biswas and Buxton 2024*a*). As T_i is increased, the individual tip vortices can still be observed (see figures 6*b* and 6*c*), but it becomes increasingly difficult to detect the merging process and the merged tip vortices. In general, as T_i is increased, the tip vortices break down much closer to the turbine as reported in previous studies (Chamorro, & Porté-Agel 2009; Wu, & Porté-Agel 2012; Gambuzza, & Ganapathisubramani 2023). For the no grid case, the wake edge towards the far wake (visually indicated by the black dash–dotted line) stays nearly flat. However, for the other cases the wake edge shows significantly larger undulation. This can be seen more clearly from the Supplementary movies 1–6. We look at the important frequencies present at different locations in the wake to better understand these primitive observations.

3.1. *Important frequencies*

In order to understand the effect of FST on the coherent motions at different frequencies, we look at the power spectral density (PSD) of transverse fluctuating velocity (PSD_v). This is first shown in the tip region close to the rotor ($x/D = 0.5$, $y/D = 0.55$) in figure 7 for the different cases (in black). Here the PSDs are estimated using Welch's method with segments of size $N/2$ (where $N = 5456$ was the length of the time series) having 50 % overlap (Welch 1967). The segments were windowed with a Hamming window. This yielded a frequency resolution of 0.0244 hz ($\Delta St_{U_\infty, D} = 0.0244$). The spectra at the same location without the turbine are also shown in blue for comparison. The Strouhal

https://doi.org/10.1017/jfm.2026.11665 Published online by Cambridge University Press

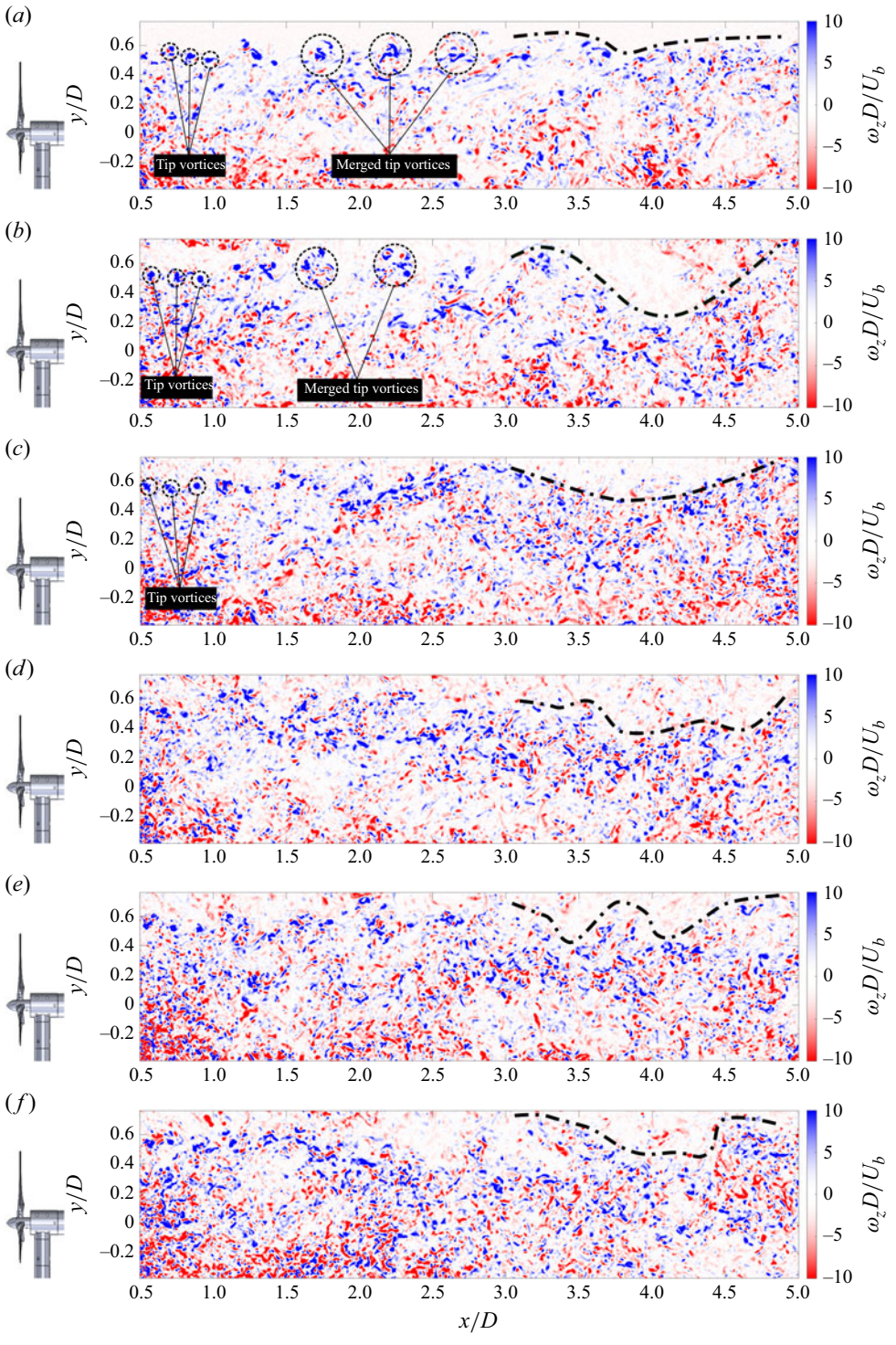


Figure 6. Exemplar instantaneous vorticity fields for the cases (*a*) 1, (*b*) 2a, (*c*) 2c, (*d*) 3b, (*e*) 4b and (*f*) 4d. The black dash–dotted line highlights the visually identified wake edge towards the far wake.

https://doi.org/10.1017/jfm.2026.11665 Published online by Cambridge University Press

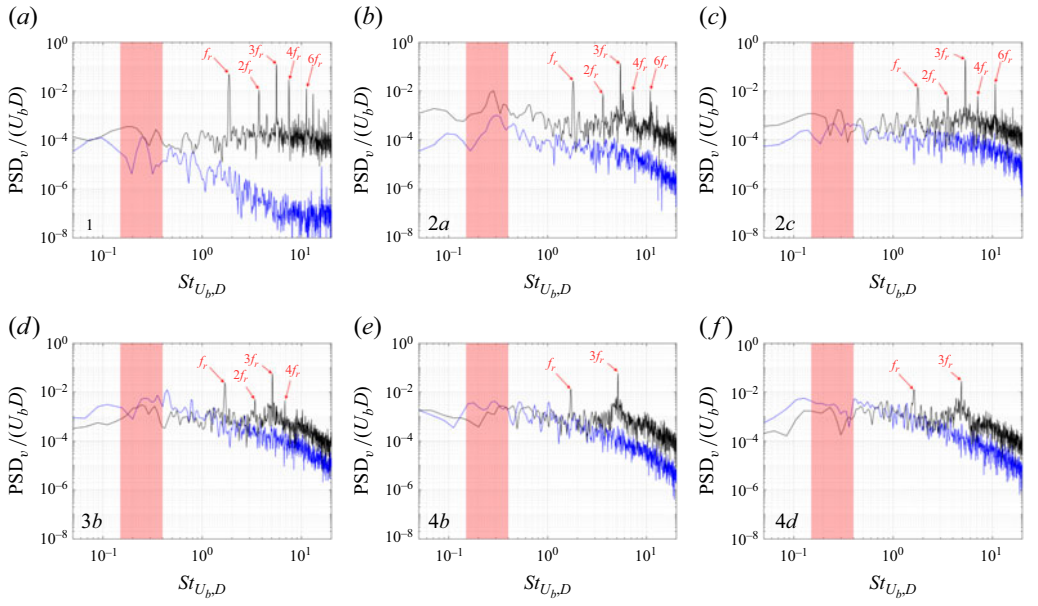


Figure 7. Spectra at $x/D = 0.5$ and $y/D = 0.55$ for the cases (*a*) 1, (*b*) 2a, (*c*) 2c, (*d*) 3b, (*e*) 4b and (*f*) 4d. The spectra with and without the turbine are shown in black and blue, respectively. The shaded region shows the WMFB ($0.15 \leqslant St_{U_b,D} \leqslant 0.4$).

number, $St_{U_b,D}$ is calculated based on the rotor averaged bulk velocity (U_b) and the turbine diameter (D). For all the FST cases, the dominant frequency is $3f_r$, where f_r is the turbine's rotational frequency ($\approx$1.87 Hz). So $3f_r$ therefore denotes the frequency of the tip vortices for a three-bladed turbine. Apart from $3f_r$, f_r is also found to be important and is observed in all cases. The harmonics of f_r up to $6f_r$ and even beyond are clearly observed for case 1. The red band in the low frequency region $0.15 \leqslant St_{U_b,D} \leqslant 0.4$ shows the typical frequency range of wake meandering reported in previous studies (Medici, & Alfredsson 2008; Chamorro *et al.* 2013; Okulov *et al.* 2014). Note that for all the cases with a turbulence generating grid, the spectral energy content in this wake meandering frequency band (WMFB) is higher than the no grid case. More interesting observations can be made by comparing the spectra at the same location without the turbine. For the cases with low FST, the turbine seems to add energy in the WMFB (figure 7*a–c*). Whilst, for medium to high FST (figure 7*d–f*), there is an attenuation of energy in the wake in this low frequency region. Especially for case 2a, there is a clear peak in the vicinity of $St_{U_b,D} \approx 0.3$ that is present both in the freestream and in the wake and is amplified in the wake. This clearly shows how the nature of the inflow turbulence can impact the low frequency wake meandering dynamics in the wake. This will be discussed in more detail in the next sections.

For the low T_i cases 2a and 2c, most of the harmonics of f_r are still observed in the tip region similar to case 1. For the medium T_i case 3b, the harmonics such as $2f_r$ and $4f_r$ are observed, but $6f_r$ is no longer observed clearly. Finally, for the highest T_i cases 4b and 4d, no spectral peaks are evident other than at f_r and $3f_r$ within the FOV considered here ($0.5 \leqslant x/D \leqslant 5$). The other frequencies can, however, still be present very close to the turbine blades.

Figure 7 showed that f_r and $3f_r$ are the only two tip vortex related frequencies that could be observed for all the FST cases. Therefore, we explore how the amplitude of

https://doi.org/10.1017/jfm.2026.11665 Published online by Cambridge University Press

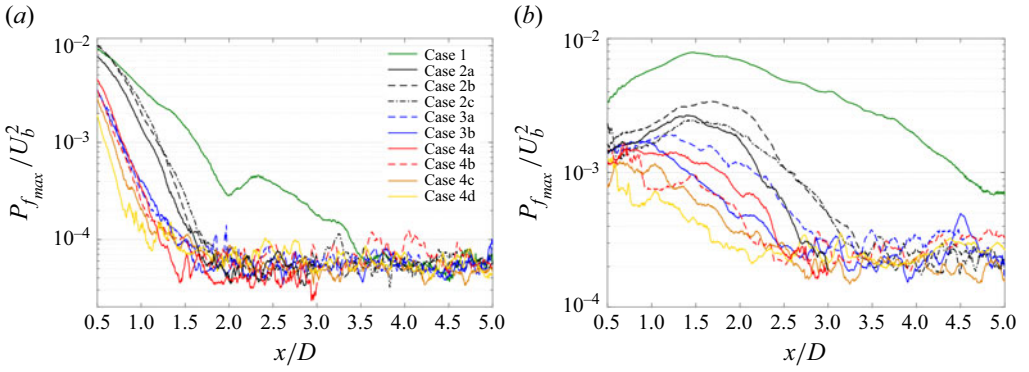


Figure 8. Maximum power of the tip vortex related frequencies (*a*) $3f_r$ and (*b*) f_r for the different FST cases.

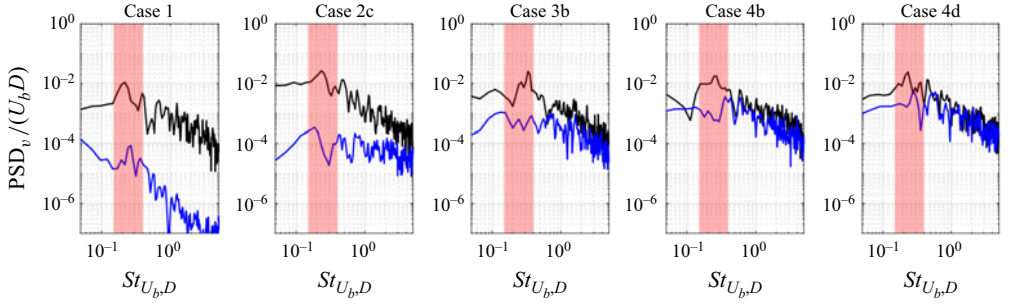


Figure 9. Spectra at $x/D = 4$ and $y/D = 0$ obtained using Welch's PSD estimator having window lengths $N/2$ for the cases 1, 2c, 3b, 4b and 4d. Here N corresponds to the total length of the time series. The windows had 50 % overlap. The spectra with and without the turbine are shown in black and blue, respectively. The shaded region shows the WMFB ($0.15 \leqslant St_{U_b,D} \leqslant 0.4$).

these two frequencies varies in the streamwise direction for the different cases. The amplitude was measured in terms of the power contained in a frequency peak ($P_f(x, y)$) at a particular location. The power was calculated by integrating the PSD over a $\Delta f = 0.14$ Hz ($\Delta St_{U_\infty,D} = 0.14$) which was the best estimate of the width of the spectral peaks associated with tip vortex related frequencies (f_r, $3f_r$, etc.). The maximum value of $P_f(x, y)$ at a particular x was taken and the streamwise variation of the maximum power ($P_{f_{max}}$) is shown in figure 8. As can be expected, $3f_r$ or the tip vortices sustain the furthest downstream for the no grid case. As the FST level is increased they decay faster and closer to the turbine. Interestingly, among the low T_i cases (group 2), $3f_r$ decays the fastest for case 2a which had the lowest T_i and the highest L_v in group 2. In fact, for the majority of the cases, the decay of $3f_r$ can be seen to be more correlated to L_v than T_i. The formation of f_r is more complex and energy can be introduced at this frequency due to for instance the blade eccentricities (very close to the turbine) and due to the merging of the tip vortices farther downstream (Abraham, & Leweke 2023; Biswas and Buxton 2024*a*). A preferred dependence on either T_i or L_v could not be observed clearly for f_r. Nevertheless, it decayed closer to the turbine with increasing FST levels.

Figure 9 shows the PSDs at $x/D = 4$ and $y/D = 0$ for the five cases (excluding case 2a) of increasing turbulence intensity. At this location, the wake meandering frequency can be expected to become important. Note that the tip vortex related frequencies always showed discrete peaks and therefore their detection was largely insensitive to how the spectrum

https://doi.org/10.1017/jfm.2026.11665 Published online by Cambridge University Press

was calculated. In contrast, the detection of the low frequency peaks in the WMFB (shown by the red shaded region in figure 9) was more sensitive to the choice of the method and the associated parameters, due to their less discrete nature. Therefore, to better understand the nature of the spectra in the WMFB, the spectra were computed with different window sizes, such as N, $N/2$ and $N/4$ (where $N = 5456$ is the length of the time series) in the Welch's method. The largest window length resulted in noisier spectra, whilst the smallest window length oversimplified the spectra (not shown here for brevity). Therefore, all the analysis related to PSDs was carried out with the intermediate window length of $N/2$ with a 50 % overlap. The final results related to wake meandering and the conclusions drawn from them were insensitive to slight departure from the chosen PSD parameters. In figure 9, clear peaks are observed in the WMFB for all the cases, even with the highest FST levels. Furthermore, the amplitude of the peak in the WMFB for all the FST cases were stronger compared with the no grid case. This is in line with the previous studies who also reported that the amplitude of wake meandering increased in the presence of FST (Espana *et al.* 2011; Gambuzza, & Ganapathisubramani 2023). The clearest peak was, however, observed for the no grid case at $St_{U_b,D} \approx 0.2$. For the other cases, this peak is less coherent or more broadband in nature. This is similar to the observation of Bourhis *et al.* (2025) who noted a broadening of the WMFB for high T_i. Note that for the no grid case, there is another peak observed at $St_{U_b,D} \approx 0.4$. This peak was likely a signature of the decaying hub vortex. Although some previous studies have found the hub vortex to become incoherent at around this location (Foti *et al.* 2016), the relatively larger nacelle used in this study likely creates a stronger hub vortex that sustains farther downstream (see for instance figures 4*c* and 4*d* of Biswas and Buxton (2024*b*)). The freestream spectra calculated at the same location are also shown in blue. Note that for all the cases, the turbine has added energy in the WMFB. The energy difference between the freestream and the wake reduces with increasing FST level. This indicates that in the central region of the far wake, wake meandering is still driven primarily by the turbine, not FST.

3.2. *Frequency maps*

For a global view of the important frequencies in different parts of the wake, a dominant frequency map is created similarly to that reported in Biswas and Buxton (2024*a*). These are shown in figure 10 for the five cases of increasing turbulent intensity. Here, we identified the dominant frequency at a spatial location based on the total power contained around that frequency. The power spectrum was integrated over a frequency window Δf centred around the frequency in question. If Δf is too large there would be non-physical contributions from different frequencies whilst a Δf too small would under predict the power in a particular coherent frequency band. $\Delta f = 0.14$ hz ($\Delta St_{U_\infty,D} = 0.14$) was chosen which was the best estimate of the width of the spectral peaks associated with tip vortex related frequencies (f_r, $3f_r$, etc.). A slight variation of Δf did not change the final nature of the maps.

The look of the maps also depends on the number/values of the contours chosen. We showed specific contours with two contours separated by a minimum of Δf, i.e. the frequencies are binned with a bin size of Δf. A frequency zone is represented just by the midfrequency in the bin with frequency boundaries $f \pm \Delta f/2$. These frequency boundaries are larger compared with the uncertainty caused by the variation in U_b for all the frequencies of importance.

The map of the non-turbulent case is shown in figure 10(*a*) and it looks similar to that reported in Biswas and Buxton (2024*a*) obtained through a different set of experiments. In figure 10(*a*), there is a small region close to the tip near the rotor where the tip vortices

https://doi.org/10.1017/jfm.2026.11665 Published online by Cambridge University Press

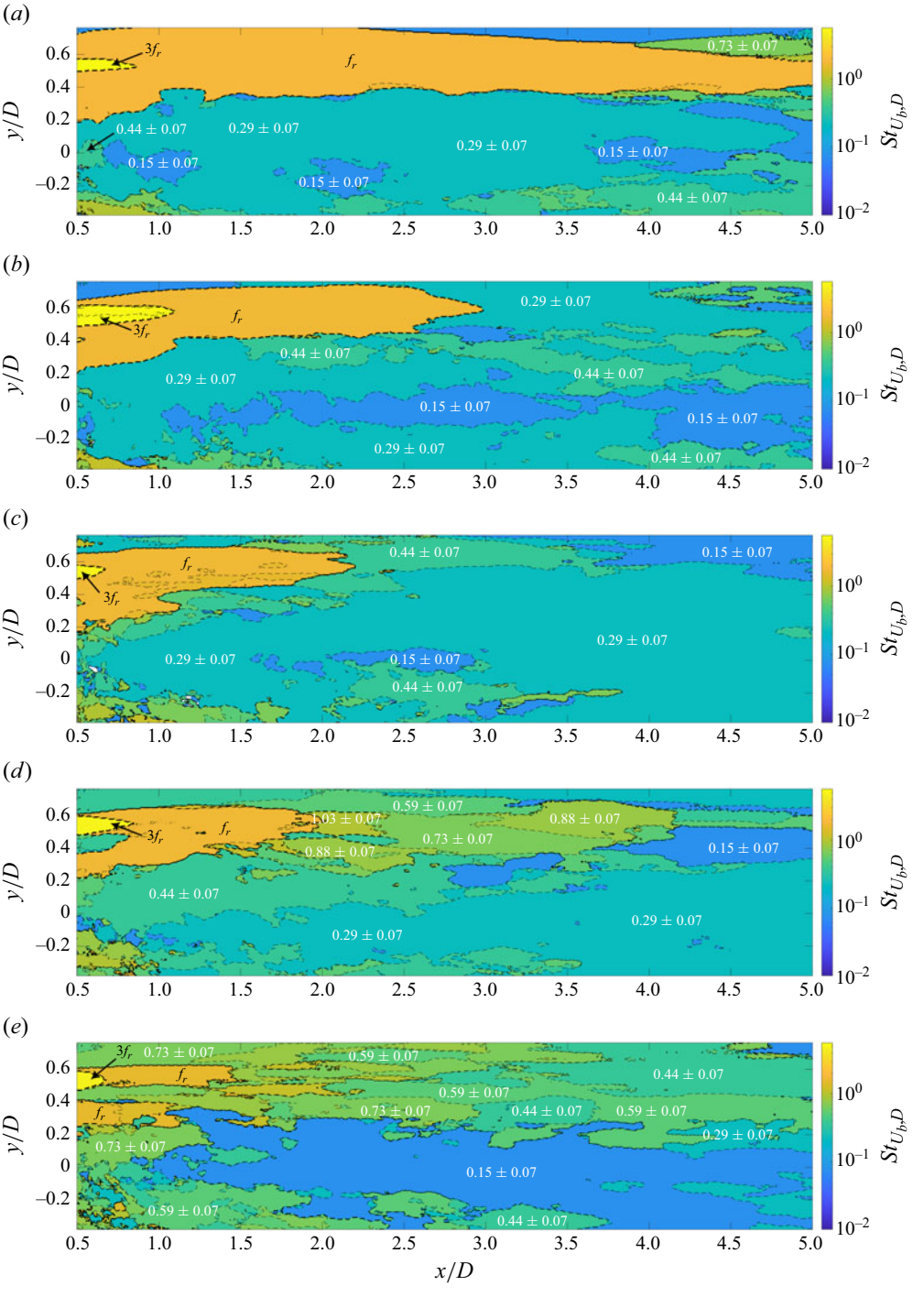


Figure 10. Dominant frequency maps for the cases (*a*) 1, (*b*) 2c, (*c*) 3b, (*d*) 4b and (*e*) 4d obtained based on the power contained in a narrow frequency band. The power spectra are obtained using Welch's PSD estimation with a window length of $N/2$ ($N = 5456$ being the length of the time series).

https://doi.org/10.1017/jfm.2026.11665 Published online by Cambridge University Press

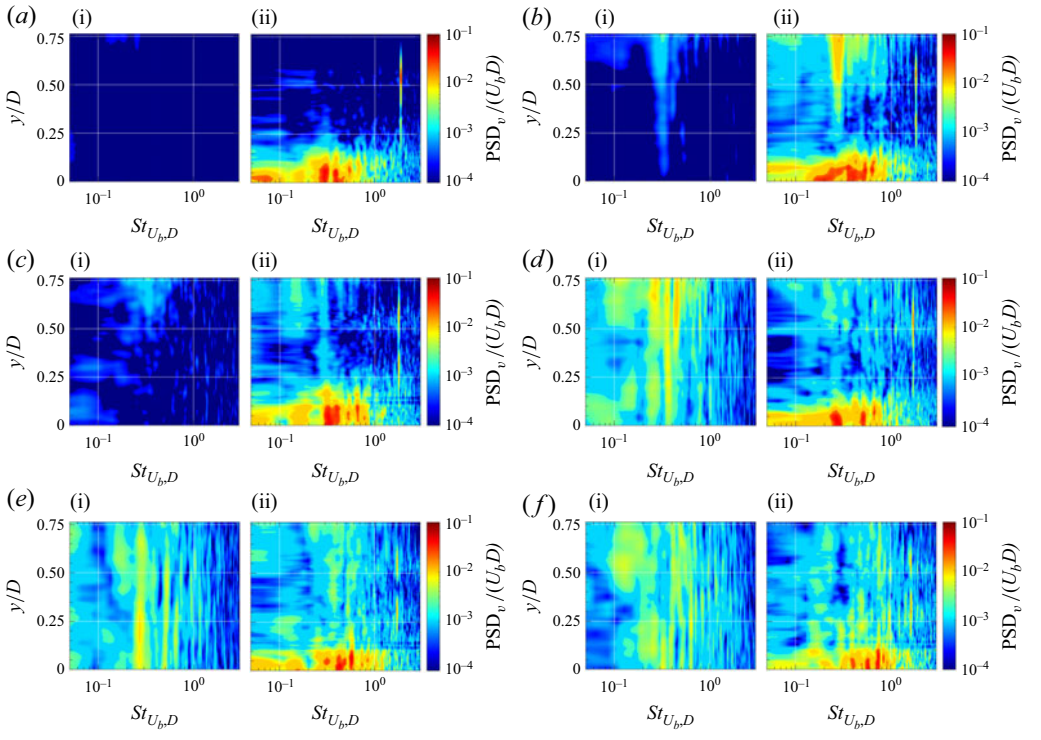


Figure 11. The PSDs $0.5D$ downstream of the turbine location for (*a*) no grid case, (*b*) case 2a, (*c*) case 2c, (*d*) case 3b, (*e*) case 4b and (*f*) case 4d, (*i*) without the turbine and (ii) with the turbine. The PSDs are obtained using Welch's PSD estimation with a window length of $N/2$.

($3f_r$) are the strongest. However, they soon interact with each other producing f_r, which remains the dominant frequency in the wake shear layer even beyond $5D$. The frequencies related to the tip vortices, especially f_r, remain dominant in a nearly axisymmetric shell type region apart from the region behind the tower (Biswas and Buxton 2024*a*). This shell type region demarcates the inner wake from the outer background fluid. In the inner wake region, multiple low frequencies dominate in large patches and these frequencies fall in the accepted frequency range of wake meandering.

For the cases with FST, the high frequency shell breaks down much closer and a connection between the outer turbulent flow and the inner wake is established much earlier. This has consequences in terms of the sustainment of wake meandering in the far wake for these cases as we will discuss. For the highest turbulence intensity cases, many new low frequencies appear in smaller patches, making it look more broadband and turbulent-like in the inner wake region as well as at the wake's outer edge. The interaction with these frequencies likely makes wake meandering more broadband in the far wake.

3.3. *The nature and amplitude of wake meandering in the presence of FST*

To elucidate the nature of wake meandering in the presence of FST, power spectral densities are shown in figure 11 with and without the turbine. Figure 11(*a* ii, *b* ii,*c* ii,*d* ii,*e* ii,*f* ii) show the spectrum in the turbine wake at a distance of $x/D = 0.5$ from the turbine itself. Figure 11(*a* i,*b* i,*c* i,*d* i,*e* i,*f* i) show the spectrum at the same location with the turbine removed. The spectra correspond to the same six cases (1, 2a, 2c, 3b, 4b and 4d) as discussed previously. The energy content in the freestream spectra

https://doi.org/10.1017/jfm.2026.11665 Published online by Cambridge University Press

is the lowest for the no grid case and it increases for the high T_i cases as expected. For all the cases in the turbine wake, low frequency peaks can be observed in the central region (near $y = 0$) in the range $0.15 \lessapprox St_{U_b,D} \lessapprox 0.4$ and $0.4 \lessapprox St_{U_b,D} \lessapprox 0.6$. The former frequency falls in the WMFB defined earlier. The latter matches well with the hub vortex or nacelle shedding frequency reported in several previous studies (Iungo *et al.* 2013; Viola *et al.* 2014; Howard *et al.* 2015; Abraham *et al.* 2019). The coexistence of the two frequencies in the vicinity of the nacelle is interesting. It is possible that the lower frequency is related to a subharmonic of the nacelle's vortex shedding that excites large-scale wake meandering downstream. This is in line with Foti *et al.* (2016) who showed that the meander profiles in the near wake ($x < 2D$) followed the hub vortex. Recently, Neunaber, Yadala & Hearst (2025) studied the interaction between a non-shedding porous disk and a solid disk shedding periodically. Interestingly, they reported that when the two were placed in a side-by-side configuration, the wake of the originally non-shedding disk acquired oscillation from the wake of the shedding disk. The wake of the porous disk was shown to be highly receptive to a range of external frequencies (provided by the solid disk). This work perfectly aligns with our idea that the nacelle's shedding likely provides an excitation to kickstart wake meandering, the only difference being that the excitation is provided internally to the wake, as opposed to the external excitation discussed in Neunaber *et al.* (2025). The turbine wake is likely receptive to frequencies in the wake meandering frequency range and it is likely the harmonic of the nacelle's shedding that provides the excitation in this case. In figure 11, some energy content is also observed in the frequency range $0.6 \lessapprox St_{U_b,D} \lessapprox 1$ which is likely associated with the altered vortex shedding from the tower (De Cillis *et al.* 2021; Biswas and Buxton 2024*a*).

The dominant wake meandering frequency in the wake core, as well as the nacelle's shedding frequency, varies with the inflow turbulence. This is likely due to the fact that FST alters the structure of the nacelle's shedding. Note that the Reynolds number based on the nacelle's diameter and U_b is $\lessapprox 7500$. In reality, the nacelle faces a much lower local velocity due to the turbine's induction effect. In any case, it is safe to say that the nacelle's Reynolds number falls in the transitional range, where the shedding frequency is sensitive to the oncoming flow. The linear stability study of Ashton *et al.* (2016) showed that inflow turbulence changed the modal structure of the nacelle's shedding/hub vortex. Although they did not report the nacelle-based Reynolds number, the turbine-diameter-based Reynolds number was 72 000, giving an impression that the nacelle-based Reynolds number was similar to our case. Similarly, a shift in the shedding frequency in the presence of FST has been observed for circular cylinders (Norberg 1986; Maryami *et al.* 2020) and axisymmetric disks (Rind, & Castro 2012). Since the nacelle's shedding provides an excitation to wake meandering, a change in the nacelle's shedding structure/frequency likely brings a slight change in the frequency of wake meandering.

Interesting observations can be made by looking at the nature of the spectra in the tip region ($y/D \approx 0.5$) in figure 11. Unlike the no grid case, for the other cases, there is a non-negligible energy content in the WMFB in the tip region (figure 11*b*–*f* ii). Interestingly, the low T_i case (case 2a) showed the highest energy content in the WMFB in the tip region (figure 11*b* ii). The spectra without the turbine (figure 11*b* i) clearly show some non-negligible energy content in almost the same frequency range that appears to have been amplified in the wake of the turbine. Curiously, there is more energy in the freestream in the WMFB for some other cases such as the 3b, 4b and 4d. However, there is a clear attenuation of the low frequencies in the wake for these cases as observed in previous studies (Chamorro *et al.* 2012; Jin *et al.* 2016). This is most likely due to the fact that for these cases, the freestream spectrum in this region is more multiscale in nature

https://doi.org/10.1017/jfm.2026.11665 Published online by Cambridge University Press

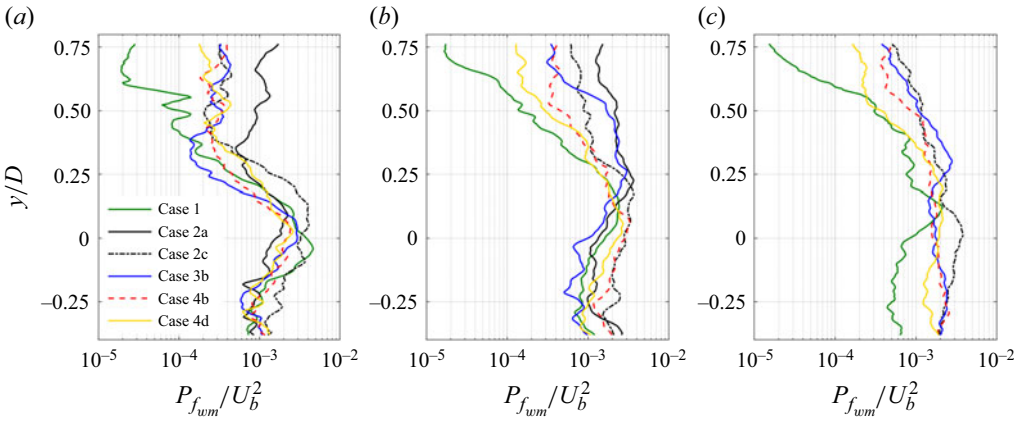


Figure 12. Transverse variation of power in WMFB for different FST cases at (*a*) $x/D = 1$, (*b*) $x/D = 3$ and (*c*) $x/D = 5$.

(presence of multiple frequencies) in contrast to more of a single frequency for case 2a. Case 2a therefore represented more of an idealised inflow where there is energy localised in a narrow band. An example of such inflow could be the flow behind a hill, where there is a coherent vortex shedding that might interact with turbines. Now, for case 2a, the turbine is placed $5D$ or $26.6M$ (M being the mesh size) behind the regular grid SRG38, where the flow should be well developed. This frequency is therefore most likely introduced by the modulation of the outer edge of the boundary layer developing on the bottom wall of the flume, although the turbine was not strictly placed within the boundary layer (please see figure 2*b*). As was discussed earlier, the grid SRG38 strongly interacted with the boundary layer. For case 2a, the distance of the rotor from the grid was the highest ($5D$) and the height of the boundary layer was also the highest $\approx 0.63D$ for this case (see figure 2*b*). Therefore, this frequency, although not strictly produced by the grid alone, shows interesting physics in this case. These observations are in line with those from recent works which suggest that the turbine has a dynamic response (Mao, & Sørensen 2018; Heisel *et al.* 2018; Gupta, & Wan 2019), i.e. the details of the inflow spectra is important in determining the wake dynamics.

It is worthwhile to note that FST can also indirectly induce/influence wake meandering through breaking down the tip vortices (Howard *et al.* 2015). Assessing the relative importance of FST in promoting wake meandering directly or indirectly through the tip vortices is non-trivial and deserves future investigations. Nevertheless, some evidence of interaction between the tip vortices and wake meandering in the presence of FST is presented in the next paragraphs.

Next, we explore how the total power in the WMFB varied for the different FST cases. The nacelle's shedding frequency at $\lambda = 6$ was previously found to be around $St_D \approx 0.42$ (Biswas and Buxton 2024*a*). Therefore, in order to avoid unwanted contributions from the nacelle's shedding frequency, the power spectra were integrated over a frequency range $0.15 \leqslant St_{U_b,D} \leqslant 0.37$ (containing $N_f \approx 10$ resolved spectral peaks) only. The wake meandering power profiles hence created are first shown at $x/D = 1$ in figure 12(*a*) for selected cases. In the central part of the wake, i.e. in the proximity of the nacelle, the power profile for the no grid case shows the strongest peak. The amplitude thereafter decays towards the edge of the wake. This reaffirms the role of the nacelle in initiating wake meandering when the FST level is negligible. For the other cases with FST, the profiles

https://doi.org/10.1017/jfm.2026.11665 Published online by Cambridge University Press

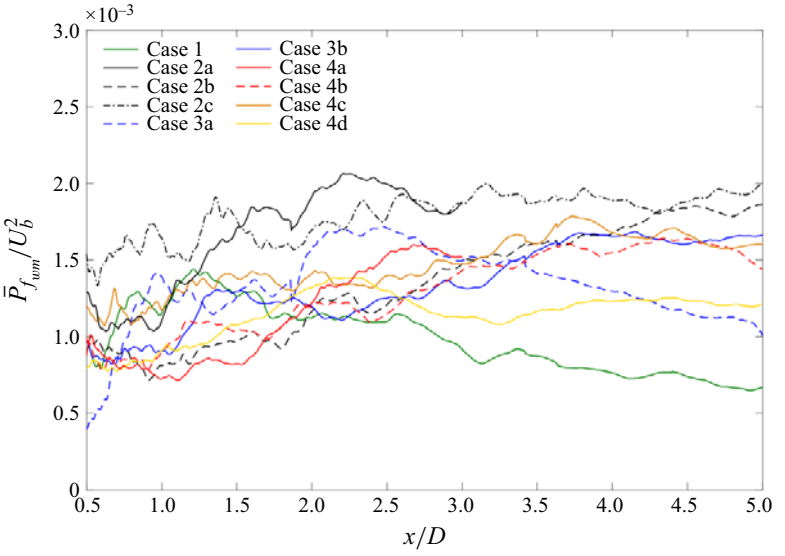


Figure 13. Streamwise variation of average power (averaged in the y direction) in WMFB for different FST cases.

still show a peak in the central region, although diminished, highlighting that the nacelle is still the key in inducing wake meandering in the central wake region for the FST cases considered here. Unlike the no grid case, however, the FST cases show non-negligible wake meandering power towards the edge of the wake. In line with the observation in figure 11(*b*), case 2a shows the highest power in the tip region in the near wake. For the middle to high FST cases, although figure 12 shows more power here compared with the no grid case, the turbine actually attenuated the power already available in the freestream in the WMFB (as was seen in figure 11). Farther downstream (figures 12*b* and 12*c*), the power in the central region diminishes for the no grid case, while that for the other cases is enhanced.

To compare all the cases simultaneously, the power profiles are averaged over y and are shown for all the cases considered here in figure 13. Note that nearer to the turbine, for $x/D \leqslant 2.5$, the average wake meandering powers are more comparable for all the cases. Beyond $x/D = 2.5$, the differences become more discernible. In particular, a monotonic decline is observed for the no grid case. Note that for the no grid case, the low frequency region in the inner wake remains shielded by the shell type region dominated by f_r (see figure 10*a*) throughout the streamwise extent of the FOV. For this case wake meandering is likely triggered by the hub vortex/nacelle's shedding and it follows a trend similar to the decay of the hub vortex (Foti *et al.* 2016). For the cases with higher FST level, the average powers of wake meandering are similar to the no grid case in the near wake. However, unlike the no grid case, farther downstream, wake meandering is sustained for the other cases. This has to do with the earlier breakdown of the tip vortices as depicted in figure 8. The breakdown of the tip vortices likely provides additional impetus to sustain far field wake meandering. Neunaber *et al.* (2020) divided the wake into four distinct regions. These included the near wake where the centreline T_i decayed (the nacelle's influence was felt) and immediately downstream, a transition region where the tip vortices break down and the shear layer starts to expand. The extents of these locations depended on the FST levels. Following the same terminology, we can say that for the cases with FST here, the transition region ensues much earlier. For the no grid case, the delayed breakup

https://doi.org/10.1017/jfm.2026.11665 Published online by Cambridge University Press

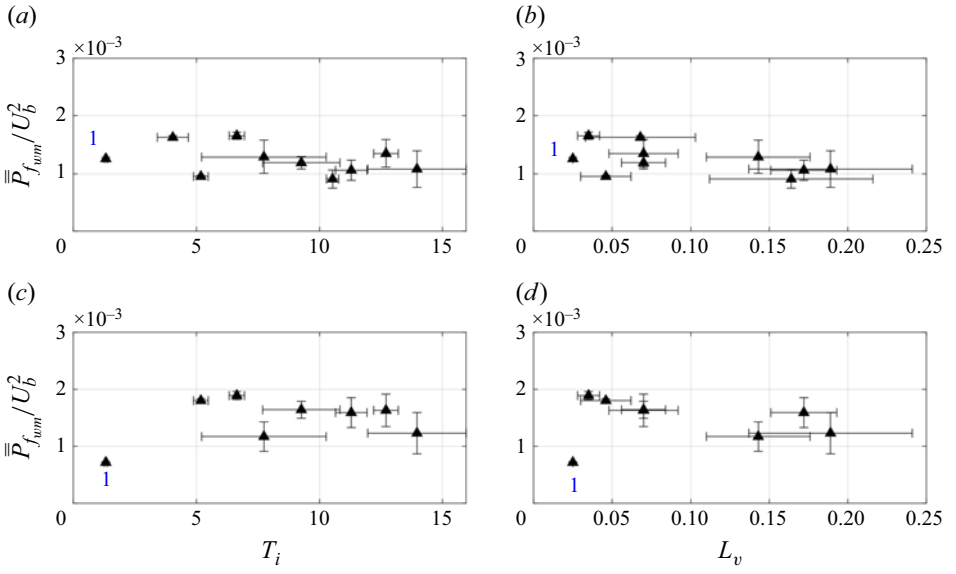


Figure 14. Variation of average power in the WMFB (*a*,*b*) in the near wake (averaged between $x/D = 1$ and $x/D = 2$) and (*c*,*d*) in the far wake (averaged between $x/D = 4$ and $x/D = 5$) for different FST cases.

of the tip vortices might eventually give a boost to wake meandering farther downstream which is not captured in the current FOV. Whether or not wake the meandering amplitude becomes comparable farther downstream is an interesting question and deserves further investigation.

To summarise the results, the spanwise averaged power curves in figure 13 are further averaged over x in the intervals $1 < x/D < 2$ (near wake) and $4 < x/D < 5$ (far wake) and shown in figure 14. In the near wake, the average powers do not show any clear trend with either T_i or L_v and are nearly the same for all the cases. This observation confirms that the primary cause of wake meandering here is the turbine itself, not the FST. Farther downstream, for all the cases with FST, the average power of wake meandering is discernibly higher than that of the no grid case. This is most likely related to the earlier breakdown of the tip vortices as we will be discussing in more detail in § 5.

A closer look at figure 7(*b*), i.e. that for case 2a at $x/D = 0.5$ and $y/D = 0.55$, reveals a new peak at a frequency slightly higher than $3f_r$. To understand the origin of this peak, the spectra are reproduced on a linear scale in figure 15(*a*). This new frequency was found to be numerically equal to $3f_r + f_{wm}$, where $f_{wm} = 0.29$ is the wake meandering frequency observed towards the outer edge of the wake. Similarly at $x/D = 0.5$ and $y/D = 0.52$, another new frequency was found which was numerically equal to $3f_r - f_{wm}$. A similar observation, although weaker, was recorded for the case 2b as well as shown in figure 15(*c*,*d*). This is an excellent example of interaction between the tip vortices and wake meandering. More interestingly, the new frequencies are similar to the secondary frequencies observed in previous studies on multiscale flows involving cylinders/prisms of unequal diameters (Baj, & Buxton 2017; Cicolin *et al.* 2021; Biswas *et al.* 2022). The secondary frequencies were numerically equal to the sum and difference of the primary shedding frequencies of the two cylinders and were shown to be produced due to the nonlinear triadic interaction between the primary frequencies. Whether the same is true for the new frequencies observed here will be explored in § 5.

https://doi.org/10.1017/jfm.2026.11665 Published online by Cambridge University Press

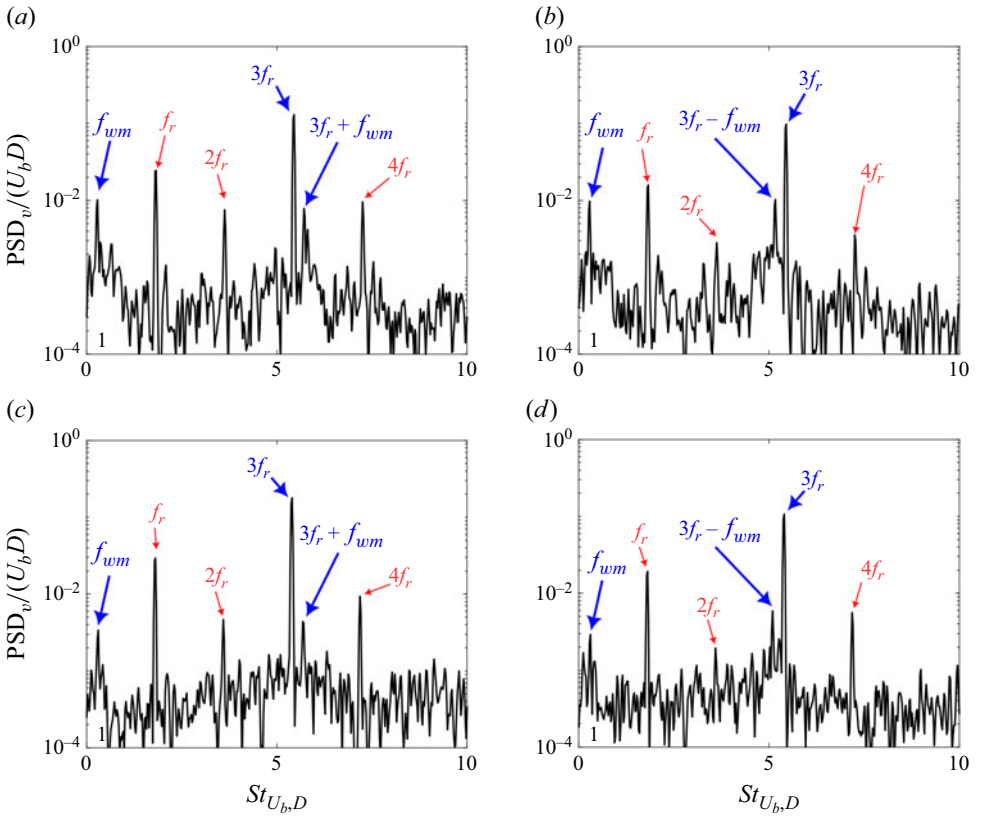


Figure 15. Spectra for case 2a at $x/D = 0.5$ and (*a*) $y/D = 0.55$ and (*b*) $y/D = 0.52$. Panels (*c*) and (*d*) show the same for the case 2b.

4. Modal decomposition

The dynamics of the various length/time scales discussed in § 3 can be better understood by distinguishing the coherent modes associated with each of them. This can be achieved through a multiscale triple decomposition of the velocity field $\boldsymbol{u}(\boldsymbol{x}, t)$ (where $\boldsymbol{x}$ and t denote space and time, respectively) in the following form:

$$\boldsymbol{u}(\boldsymbol{x}, t) = \bar{\boldsymbol{u}}(\boldsymbol{x}) + \sum_l \tilde{\boldsymbol{u}}_l(\boldsymbol{x}, t) + \boldsymbol{u}''(\boldsymbol{x}, t). \tag{4.1}$$

Here $\bar{\boldsymbol{u}}(\boldsymbol{x})$ is the mean component, $\boldsymbol{u}''(\boldsymbol{x}, t)$ is the stochastic component and $\sum_l \tilde{\boldsymbol{u}}_l(\boldsymbol{x}, t)$ represents the sum of velocity modes corresponding to individual coherent structures in the flow. The coherent velocity modes ($\tilde{\boldsymbol{u}}_l(\boldsymbol{x}, t)$) can be obtained using a data-driven modal decomposition technique such as proper orthogonal decomposition (POD), dynamic mode decomposition (DMD), or some variant of the two (Sirovich 1987; Schmid 2010; Wynn *et al.* 2013).

Such data-driven modal decomposition techniques have been applied on a wind turbine wake (Sarmast *et al.* 2014; Debnath *et al.* 2017; De Cillis *et al.* 2021; Biswas and Buxton 2024*b*). These methods successfully captured the modes related to tip vortices and vortex sheddings from the tower or nacelle and wake meandering (Debnath *et al.* 2017; De Cillis *et al.* 2021; Kinjangi, & Foti 2023; Biswas and Buxton 2024*b*). For the current dataset, we use optimal mode decomposition (OMD) which is a more generalised version

https://doi.org/10.1017/jfm.2026.11665 Published online by Cambridge University Press

of the originally proposed DMD algorithm (Schmid 2010; Wynn *et al.* 2013). The DMD assumes that there is a linear dependency between two successive snapshots ($\boldsymbol{v_n}$, $\boldsymbol{v_{n+1}}$) of the flow which remains constant over time. This can be written as

$$\boldsymbol{v_{n+1}} = \boldsymbol{A}\boldsymbol{v_n}, \qquad \boldsymbol{A} \in \mathbb{R}^{p\times p}. \tag{4.2}$$

Here p denotes the length of a snapshot (the number of PIV vectors). The DMD finds $\boldsymbol{A}$ by solving the minimisation problem:

$$\min \quad \left\| [\boldsymbol{v_2}, \ldots \boldsymbol{v_N}] - \boldsymbol{A}[\boldsymbol{v_1}, \ldots \boldsymbol{v_{N-1}}] \right\|^2. \tag{4.3}$$

Here, N is the number of PIV snapshots. In OMD, $\boldsymbol{A}$ is represented in a rank constrained form ($\boldsymbol{LML^T}$) and a two-way optimisation is performed (with optimisation variables $\boldsymbol{L}$ and $\boldsymbol{M}$):

$$\begin{aligned} \min \quad & \left\| [\boldsymbol{v_2}, \ldots \boldsymbol{v_N}] - \boldsymbol{LML^T}[\boldsymbol{v_1}, \ldots \boldsymbol{v_{N-1}}] \right\|^2 \\ \text{s.t.} \quad & L^T L = I \\ & M \in \mathbb{R}^{r\times r}, \quad L \in \mathbb{R}^{p\times r} \end{aligned} . \tag{4.4}$$

Here, $\boldsymbol{L}$ represents the low-order subspace of the flow field and $\boldsymbol{M}$ represents the dynamics of $\boldsymbol{L}$. r denotes the rank of LML^T and is a fixed chosen parameter. Wynn *et al.* (2013) showed that in DMD, $\boldsymbol{L}$ was taken as the POD subspace of the flow. Thereafter, the best dynamical representation ($\boldsymbol{M}$) of the flow on that subspace was obtained. Wynn *et al.* (2013) argued that the POD subspace is not necessarily the best choice for $\boldsymbol{L}$, hence suggesting a more general, two-way optimisation. Finally, after finding the eigenvectors ($\boldsymbol{z_m}$) and eigenvalues (γ_M) of $\boldsymbol{M}$, the OMD eigenvectors ($\boldsymbol{\phi_{OMD}}$) and eigenvalues (γ_{OMD}) are obtained as

$$\boldsymbol{\phi_{OMD}} = \boldsymbol{L}\boldsymbol{z_M}, \qquad \gamma_{OMD} = \log(\gamma_M)/\Delta t. \tag{4.5}$$

Here, Δt corresponds to the time period between two consecutive snapshots.

Wynn *et al.* (2013) showed that the restrictive nature of DMD can result into significant under performance in some cases compared with OMD. In our previous work, we compared the performance of OMD with POD in a different flow considering the wake of a multiscale array of bars (Baj *et al.* 2015). The POD was found to be incapable of correctly identifying the mode shapes farther downstream from the wake generating body. Therefore, OMD was the preferred choice.

The OMD modes are complex and appear in conjugate pairs. The associated complex time varying coefficients, a and a^* are obtained by projecting the velocity snapshots onto the OMD modes. Finally, the physical velocity field associated with a mode, i.e. $\tilde{\boldsymbol{u}}_l(\boldsymbol{x}, t)$ is obtained through a linear combination of the OMD mode and its coefficient as $\tilde{\boldsymbol{u}}_l(\boldsymbol{x}, t) = a \times \boldsymbol{\phi}_{OMD} + a^* \times \boldsymbol{\phi}^*_{OMD}$. Note that the real and imaginary parts of the eigenvalues (γ_{OMD}) associated with the OMD modes correspond to the growth rate and the frequency of the OMD modes, respectively. A mode with a higher growth rate and a physically meaningful spatial mode shape is defined as a coherent mode in this study. However, note that the growth rates are used merely as an indicator, the OMD eigenvalues are not used to construct the time dynamics of the modes.

Biswas and Buxton (2024*b*) recently applied OMD to the wake produced by the same wind turbine model as in the present study. Various coherent modes such as the ones associated with the tip vortices, the vortex sheddings from the nacelle and the tower and wake meandering were identified and the effect of the tip speed ratio was discussed. However, the analysis was restricted to the case with negligible FST. In this section, we build on the results of Biswas and Buxton (2024*b*) by including the effect of FST.

https://doi.org/10.1017/jfm.2026.11665 Published online by Cambridge University Press

4.1. *Mode clustering*

The OMD was performed with a rank $r = 175$ to be consistent with our previous work (Biswas and Buxton 2024*b*). For brevity, the typical OMD spectra are only shown for four selected cases: 1 (no grid case), 2c, 3b and 4b in figures 16(*a*), 16(*d*), 16(*g*) and 16(*j*). Due to the discrete nature of the tip vortex related frequencies, their identification from the OMD spectra was straightforward. However, it was not so for the low frequency wake meandering related modes. In the vicinity of the WMFB, i.e. in $0.15 \leqslant St_D \leqslant 0.4$, there were multiple modes with comparable frequencies and growth rates. The associated mode shapes also looked similar. This was more of a problem for the cases with medium to high FST levels for which wake meandering became an increasingly broadband phenomenon. Therefore, in order to simplify the OMD spectra (especially in the vicinity of the WMFB), the spatially (and spectrally) similar modes were identified and grouped together into a single representative mode. As we will show in the following section, this clustering approach ultimately helps us to examine the energy exchanges to/from the broader band wake meandering observed in the presence of FST.

Beit-Sadi, Krol & Wynn (2021) proposed a clustering algorithm that grouped/clustered similar OMD modes together to form a smaller set of dissimilar modes. The authors used graph theory to cluster the modes in an iterative process. To assess the similarity of two modes, the authors looked at the similarity between the subspaces spanned by the real and imaginary parts of the complex OMD modes. A constraint based on spectral similarity was also imposed. Finally, two modes were considered to be similar if the spatial and spectral similarity was above a threshold value. The algorithm was later successfully applied to construct the shedding modes behind a cylinder exposed to FST (de Oliveira *et al.* 2025). We apply the same algorithm for this case, albeit with some changes in the way the similar modes are grouped. The method is discussed in detail in Appendix B.

The evolution of the OMD spectra at the first, second and the final iterations of clustering is shown in figure 16 for the four selected cases. For each case, a sensitivity analysis was performed to select a threshold value/cutoff for spatial and spectral similarity (denoted by ζ_{spat} and ζ_{spec}, respectively). This is discussed in Appendix B (please see figure 25). After finding the similar modes, they are connected with an 'edge' (shown by the black lines) in figure 16. Note that there exists a number of similar modes only in the vicinity of the WMFB. Once the similar modes are identified, the problem of clustering becomes equivalent to finding subgroups/clusters where each mode is connected with every other mode with an edge. In addition, a subgroup should not be strictly contained in another group. In order to obtain the mode representing a cluster, the modes in the same cluster are multiplied with a weight (related to the growth rate of the modes) and stored in a matrix. Thereafter, the first singular value of the matrix is simply used to represent the mode associated to the cluster. The modes representing a cluster are also assigned a virtual growth rate and a frequency which is obtained by taking a weighted average of the frequencies and growth rates of the modes forming a cluster. Please refer to Appendix B for further details.

Interestingly, a significant number of similar modes are observed for the no grid case as well. Note that, the recent work by Biswas and Buxton (2024*b*) applied OMD on the same data set as case 1 here without mode clustering. The modes obtained with/without mode clustering were similar for the no grid case as will be discussed in the next paragraph. Mode clustering therefore simplified the spectrum in the present case, making it easier to select the physically meaningful modes which are used to form a reduced-order representation of the coherent component of the flow. Further details about the mode selection process can be found in Appendix C.

https://doi.org/10.1017/jfm.2026.11665 Published online by Cambridge University Press

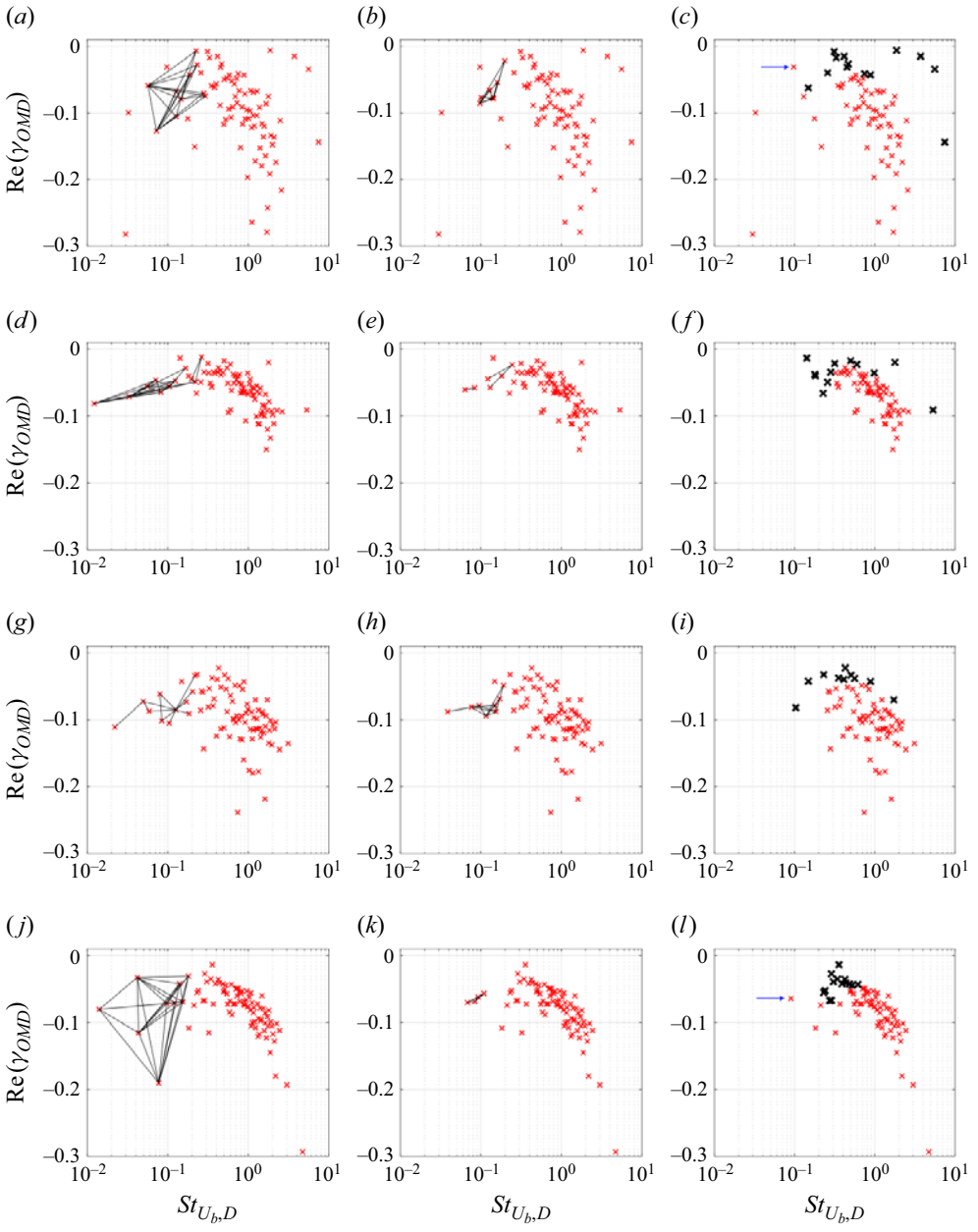


Figure 16. First, second and final iterations of the mode clustering algorithm for the no grid case (*a–c*), case 2c (*d–f*), case 3b (*g–i*) and case 4b (*j–l*). The similar modes are connected with a black solid line. The modes selected in the reduced-order representation are marked by the '×' symbols. The modes indicated by the blue arrows were not selected despite being less damped since the associated mode shapes could not be interpreted as physically meaningful.

Upon clustering, the selected modes are highlighted in figures 16(*c*), 16(*f*), 16(*i*) and 16(*l*) with the '×' symbols. Among the tip vortex related modes, only the frequencies $f_r - 4f_r$ could be captured in the OMD spectrum (figure 16*c*). The higher harmonics, $5f_r$ and $6f_r$ are weaker in nature and are concentrated close to the rotor. Biswas and

https://doi.org/10.1017/jfm.2026.11665 Published online by Cambridge University Press

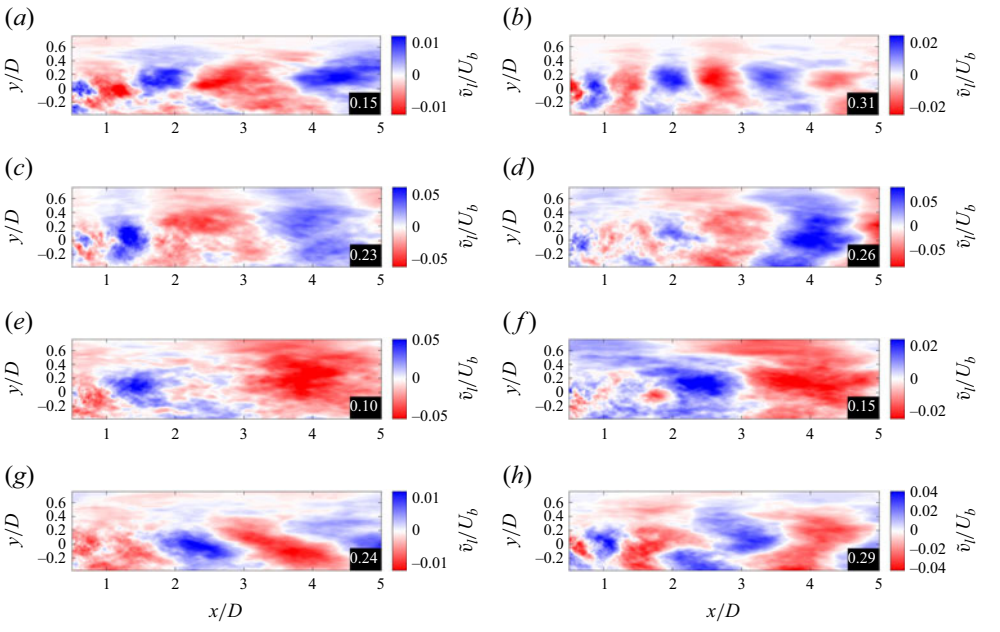


Figure 17. Two dominant wake meandering modes for the cases (*a*,*b*) 1, (*c*,*d*) 2c, (*e*,*f*) 3b, (*g*,*h*) 4b. The associated Strouhal numbers ($St_{U_b,D}$) are also highlighted in the figures at the bottom right-hand corners.

Buxton (2024*b*) could not detect these frequencies in the OMD spectra even with a higher rank of the OMD matrices. The modes corresponding to these frequencies were therefore obtained using phase averaging. The snapshots were divided into 48 phase bins (with phases ranging from $-\pi$ to π) at the reference frequency. Subsequently, the second Fourier mode of the phase-averaged flow field was taken in order to produce a complex spatial mode that mimics the OMD modes (Baj, & Buxton 2017; Biswas *et al.* 2022). For all cases, the final modes (marked by the '×' symbols) were carefully selected by looking at the spatial mode shape and how the clusters evolved over iterations. The time-varying coefficients of the modes were obtained by projecting the snapshots onto the selected modes.

4.2. *The nature of the wake meandering mode in the presence of FST*

The transverse velocity component ($\tilde{v}_l$, where l runs over the coherent modes) of the two dominant wake meandering modes (having a frequency in the WMFB) for the four cases of increasing T_i are shown in figure 17. For the no grid case (figures 17*a* and 17*b*), regular patterned structures of wavelength $1.5-2D$ are observed. The modes start from close to the nacelle in the inner part of the wake and expand farther downstream. Note that, these two modes are almost exactly the same as the modes reported by Biswas and Buxton (2024*b*) without mode clustering (see figures 4*a* and 4*b*), apart from a slight phase shift and a slight difference in the mode amplitude. This offers reassurance that the mode clustering algorithm adopted here does not alter the physical information embedded in the data set, rather it simplifies the analysis. For case 2c (low T_i), the dominant wake meandering modes in figures 17(*c*) and 17(*d*) still show similar regular structures, but the modes exhibit a larger transverse (along y) width compared with that for the no grid case. Note from figures 17(*a*) and 17(*b*) that the modes for the no grid case are not particularly

https://doi.org/10.1017/jfm.2026.11665 Published online by Cambridge University Press

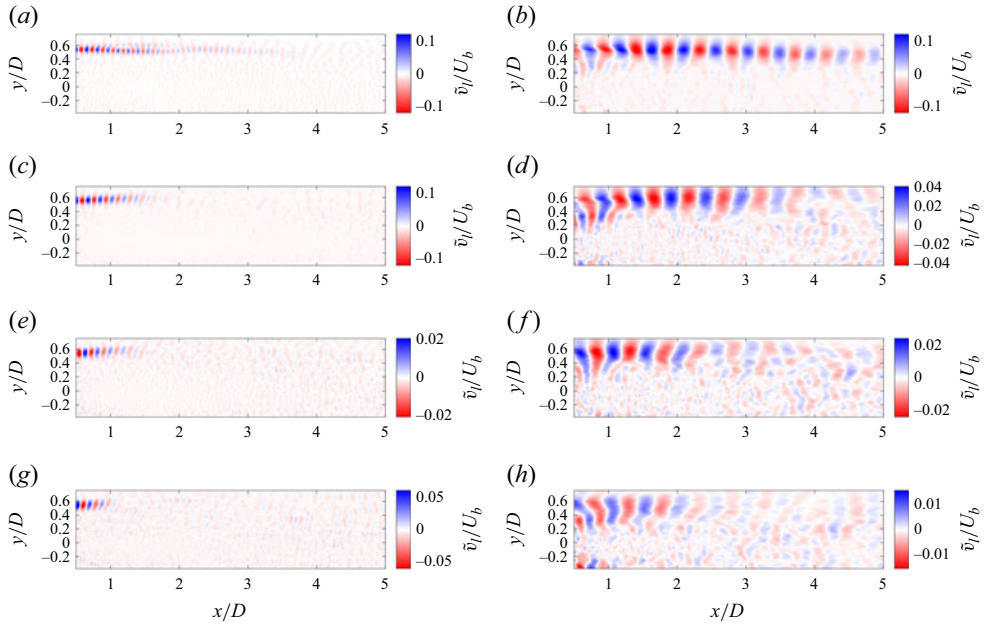


Figure 18. Modes associated with $3f_r$ (a,c,e,g) and f_r (b,d,f,h) for the no grid case (a,b), case 2c (c,d), case 3b (e,f) and case 4b (g,h).

energetic for $y \geqslant 0.5D$. The modes initiate from the vicinity of the nacelle highlighting the importance of the nacelle to providing the perturbation necessary to kick start wake meandering (Howard *et al.* 2015; Biswas and Buxton 2024*a*). For higher T_i, the modes show a significant energy content for $y \geqslant 0.5D$ as was discussed in § 3. They also become increasingly irregular in nature with increasing FST levels. A higher transverse width of the modes can, however, still be observed, at least for the medium T_i case (case 3b).

The energy budget analysis in Biswas and Buxton (2024*b*) revealed that in the absence of FST, the wake meandering modes were primarily energised by the mean flow. In the presence of FST, whether the dominant energy source for the mode stays the same or not is an interesting question and it will be discussed further in the following sections.

4.3. *The modes related to the tip vortices*

Among the tip vortex related frequencies, only the modes associated with $3f_r$ and f_r are shown in figure 18 for the same four cases (1, 2c, 3b, 4b) since they were the most important and were observed for all the cases (see figure 7). The modes associated with $3f_r$ clearly show how the tip vortices break down earlier as FST intensity is increased. A similar pattern is observed for the modes associated with f_r as well as the harmonics of f_r and $3f_r$ (not shown for brevity). Furthermore, the modes with FST appear to have a larger transverse spread. This is likely due to the vortex wandering or vortex jittering reported in previous studies in the presence of FST (Gambuzza, & Ganapathisubramani 2023).

Note that for the cases 2a and 2b, new frequencies were observed that corresponded to the sum and difference of $3f_r$ and a wake meandering frequency that was dominant near the edge of the wake. These frequencies were, however, not present in the OMD spectrum for either of the cases. A similar observation was reported in our previous studies where the new frequencies corresponding to the sum and difference of the dominant coherent

https://doi.org/10.1017/jfm.2026.11665 Published online by Cambridge University Press

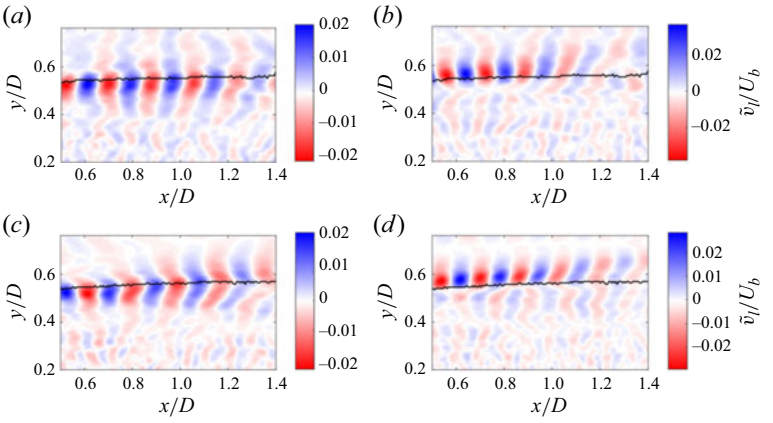


Figure 19. Modes associated with $3f_r - f_{wm}$ (*a*,*c*) and $3f_r + f_{wm}$ (*b*,*d*) case 2a (*a*,*b*) and case 2b (*c*,*d*).

modes were not captured by OMD (Baj, & Buxton 2017; Biswas *et al.* 2022). These modes therefore had to be obtained using phase averaging. These are shown in figure 19 for cases 2a and 2b. The spatial orientation of the modes reveals an interesting pattern. Note from figure 11(*b*) that the f_{wm} mode interacting with $3f_r$ was energetic in the freestream side ($y > 0.5D$). In order to indicate the difference in the spatial location of the modes, a black line was added to figure 19 showing the loci of the points where the kinetic energy of the mode $3f_r$ was maximum. It can be seen that for both the cases, the high frequency mode $3f_r + f_{wm}$ is situated more towards the freestream side, while $3f_r - f_{wm}$ resided more towards the wake side. The exact same spatial orientation was observed for secondary frequencies in fundamentally different multiscale flows (Baj, & Buxton 2017; Biswas *et al.* 2022). Biswas *et al.* (2022) considered the wake of a cylinder (main cylinder) and control rod (another cylinder of diameter 1/10th of the main cylinder). Apart from the shedding modes associated with the main cylinder (f_m) and control rod (f_c), secondary frequencies $f_c \pm f_m$ were observed. The high frequency mode resided more towards the shear layer between the two wake generating bodies, while the low frequency mode resided in the other outer side of the wake of the smaller wake generating body (having a higher shedding frequency). A similar observation was reported by Baj & Buxton (2017) in the wake of a multiscale array of prisms. These secondary frequencies were shown to be a result of nonlinear triadic interaction between the two primary shedding frequencies. The fact that we observe such similarity between simple two-dimensional multiscale flows and a complex three-dimensional multiscale flow involving rotation is truly remarkable and adds credence to the notion that these multiscale interactions are indeed universal.

5. Energy exchanges

In this section, we use the multiscale triple-decomposed coherent kinetic energy budget equation derived by Baj & Buxton (2017) to assess the energy budgets of the individual coherent modes. Baj & Buxton (2017) derived separate equations for the kinetic energy associated with the mean flow ($\bar{k}$), each of the coherent modes ($\tilde{k}_l$ for the l_{th} coherent mode) and the stochastic component of the flow (k''). For the present work, we only use the equation for the coherent modes which can be symbolically represented as the following:

https://doi.org/10.1017/jfm.2026.11665 Published online by Cambridge University Press

$$\frac{\partial \tilde{k}_l}{\partial t} = -\tilde{C}_l + \tilde{P}_l - \hat{P}_l + \left(\tilde{T}_l^{+} - \tilde{T}_l^{-}\right) - \tilde{\epsilon}_l + \tilde{D}_l. \tag{5.1}$$

Here, the source terms on the right-hand side consist of convection ($\tilde{C}_l$), mean flow production ($\tilde{P}_l$) or energy transfer from the mean flow to the l_{th} coherent mode, production of stochastic turbulent kinetic energy directly from the coherent mode l ($\hat{P}_l$), triadic energy production ($\tilde{T}_l^{+} - \tilde{T}_l^{-}$), direct dissipation from coherent mode l ($\tilde{\epsilon}_l$) and diffusion ($\tilde{D}_l$). Note that this equation is directly derived from the Navier–Stokes equations. Here, the triple decomposed velocity field (4.1) is plugged into the momentum equations and a time average is taken after multiplying with the velocity component of the l_{th} coherent mode ($\tilde{u}_l$). Therefore, all the terms in (5.1) are averaged over time. On the left-hand side, $\partial \tilde{k}_l/\partial t$ is essentially zero. The formulation of the equations as they are presented means that they are extensible to for example an unsteady Reynolds-averaged Navier–Stokes type paradigm. Baj & Buxton (2017) showed that the triadic energy production term can become significant only when there exist three frequencies that linearly combine to zero or, in other words, there is a triad in the form $f_l \pm f_s \pm f_t = 0$. The constituents of this term were defined as follows:

$$\tilde{T}_l^{+} = -\frac{1}{2} \sum_{f_s, f_t} \overline{\tilde{u}_i^{f_l} \tilde{u}_j^{f_t} \frac{\partial \tilde{u}_i^{f_s}}{\partial x_j}}, \qquad \tilde{T}_l^{-} = -\frac{1}{2} \sum_{f_s, f_t} \overline{\tilde{u}_i^{f_s} \tilde{u}_j^{f_t} \frac{\partial \tilde{u}_i^{f_l}}{\partial x_j}}. \tag{5.2}$$

Here, the overbars denote time averaging. Here $\tilde{T}_l^{+}$ denotes the total nonlinear energy transfer from f_s to f_l, while $\tilde{T}_l^{-}$ denotes the energy lost by f_l to f_s. In both these terms, f_t acts as a mediator or a catalyst (Baj, & Buxton 2017; Yeung *et al.* 2024). Here $\tilde{u}_i^{f_l}$ denotes the i_{th} velocity component of the coherent mode l (having frequency f_l). The total triadic energy gain/loss for f_l is obtained by summing over all the frequencies (f_s, f_t) that form a triad with f_l. The other term that is of particular interest is the $\tilde{P}_l$ term since it is directly linked to wake recovery. Here $\tilde{P}_l$ is defined as $\tilde{P}_l = -\sum_m \overline{\tilde{u}_i^m \tilde{u}_j^l}(\partial \overline{u}_i/\partial x_j)$, where m can be any coherent mode selected in the reduced-order representation of the flow including the l_{th} mode. The complete composition of each of the terms of (5.1) can be found in Baj & Buxton (2017).

Biswas and Buxton (2024*b*) recently used this equation to obtain the energy budget terms of each of the individual coherent modes in a wind turbine wake with negligible FST. It was reported that the modes associated with the nacelle/tower's vortex shedding and wake meandering were energised by the mean flow. Contrastingly, the tip vortex related modes could be energised through different pathways such as energy transfer from the mean flow or nonlinear triadic interactions between various coherent modes coexisting in the wake. The role of the triadic interactions in the tip vortex stability and merging process was quantified for the first time. Yeung *et al.* (2024) recently proposed a triadic orthogonal decomposition which identified coherent structures that optimally account for triadic interactions and quantified the triadic energy transfers. The authors used the same PIV dataset obtained by Biswas and Buxton (2024*b*) and reported that the energy transfers obtained using the new method were in good agreement with the previous work. Although these studies have significantly improved our understanding of the origin and evolution of the various coherent structures in a wind turbine wake, the effect of FST was not considered in these studies. This section attempts to fill that gap.

The kinetic energy budget terms are first discussed for the four cases analysed previously. The energy budget terms are summed over the entire domain and shown in

https://doi.org/10.1017/jfm.2026.11665 Published online by Cambridge University Press

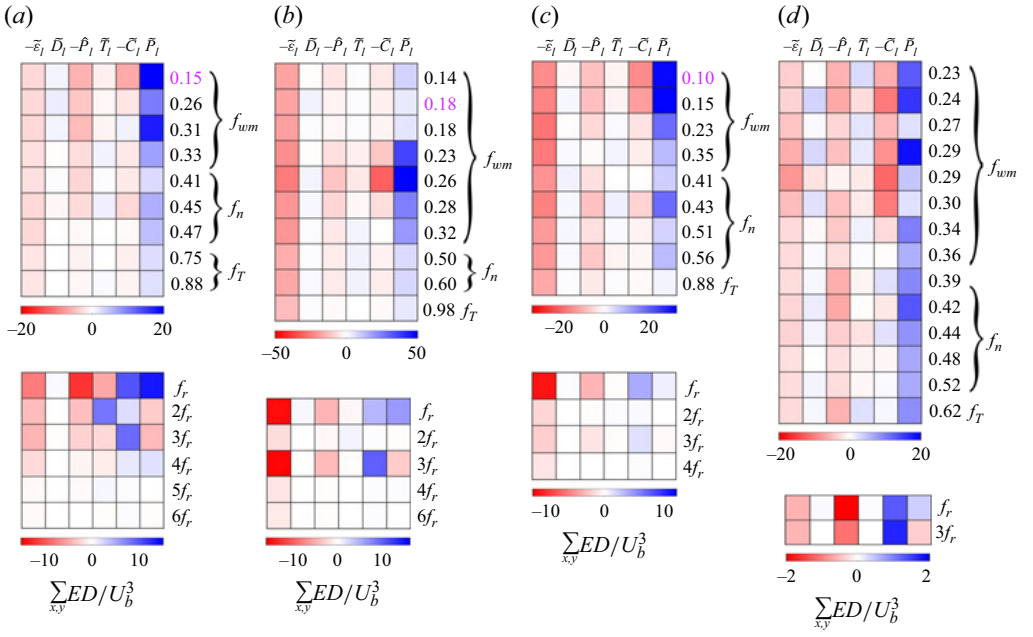


Figure 20. Summed budget terms for (*a*) no grid case, (*b*) case 2c, (*c*) case 3b and (*d*) case 4b. The numbers on the right show the associated Strouhal numbers ($St_{U_b,D}$) of the modes. For the clustered modes, the $St_{U_b,D}$ values are highlighted in purple. Here E is a generic variable representing the budget terms.

figure 20. Since the modes related to the tip vortices show weaker energy exchanges compared with the low frequency modes, a separate colour bar is used for them. On the right, the numbers show the Strouhal numbers ($St_{U_b,D}$) associated with the modes. The modes are also classified as either related to wake meandering ($0.15 \leqslant f_{wm} \leqslant 0.4$), nacelle's shedding ($0.4 \leqslant f_n \leqslant 0.6$) or the tower's shedding ($0.6 \leqslant f_T \leqslant 1$) as discussed in § 3.1. On some occasion this classification could not be made strictly based on the frequency, particularly for the clustered modes. As already discussed, for these modes, the frequency associated with the cluster was obtained as a weighted average of the frequencies of the modes forming the cluster (which may differ from the actual frequency of the mode). Therefore, the clustered modes were carefully classified by looking at their mode shape and the frequency content in the associated time varying mode coefficient. An example can be seen in figure 20(*c*), where $St_{U_b,D} = 0.1$ was classified as related to wake meandering.

Biswas and Buxton (2024*b*) showed that in the presence of negligible FST, the wake meandering mode acted like a 'primary mode', extracting energy from the mean flow. In the presence of FST, the mean flow production ($\tilde{P}_l$) term is still found to be the dominant energy source for wake meandering. The $\tilde{P}_l$ terms for the dominant wake meandering modes in the presence of FST were always found to be stronger than that for the no grid case which is in line with the discussion in § 3. Furthermore, the dominant wake meandering modes for case 2c drew the highest amount of energy from the mean flow. This is in line with the highest far wake meandering amplitude seen for this FST case in figure 13. The $\tilde{P}_l$ term then became relatively weaker as T_i was increased further, likely due to the wake meandering modes becoming less coherent (as observed in figure 17) and less efficient at extracting energy from the mean flow. This was accompanied by an

https://doi.org/10.1017/jfm.2026.11665 Published online by Cambridge University Press

enhancement in the relative contributions from the triadic interaction and diffusion term for the highest T_i case.

The tip vortex related modes in the presence of FST showed energy exchanges similar to the no grid case, however, the magnitudes of the terms decreased as T_i was increased. f_r for the no grid case was primarily energised by the mean flow production ($\tilde{P}_l$) term. For the cases 3b and 4b, the relative contribution of the convection term for f_r was higher than the $\tilde{P}_l$ term. As T_i is increased, the location where the kinetic energy of the f_r mode is maximum moves farther upstream. Therefore a larger proportion of the $\tilde{P}_l$ is not captured within the PIV FOV and eventually this missing energy is 'picked up' by the convection term. A FOV large enough to capture the full spatial growth and decay of the mode would yield zero total convection. Note that the tip vortices ($3f_r$) are formed due to the difference in pressure between the pressure and suction surface of the blades (Andersen *et al.* 2013). So $3f_r$ is therefore energised upstream of the FOV and simply decays (due to different energy transfers) within the FOV under consideration. Interestingly, the $2f_r$ mode was found to be energised by the triadic interaction term for all the FST cases in which it could be captured. A similar observation was reported by Biswas and Buxton (2024*b*) when FST was negligible. So $2f_r$ was therefore identified as a secondary mode that is produced purely due to nonlinear interaction. The magnitude of the triadic interaction term diminished drastically with T_i indicating weaker nonlinear interaction. For the highest T_i cases, the harmonics of f_r and $3f_r$ were not observed within the FOV and hence no triadic interaction could be captured.

The intriguing question is why is the $\tilde{P}_l$ term at all stronger for the wake meandering modes in the presence of FST? To answer this we need to look at the composition of the $\tilde{P}_l$ term. As discussed in Biswas and Buxton (2024*b*), utilising the fact that the transverse gradient of streamwise mean velocity ($\partial\bar{u}/\partial y$) is much stronger than the other mean velocity gradients and assuming that the velocity components of the different modes are uncorrelated ($\overline{\tilde{u}^l\tilde{v}^n} \approx 0$), we can approximate the mean flow production term as $\tilde{P}_l \approx -\overline{\tilde{u}^l\tilde{v}^l}\partial\overline{u}/\partial y$. This was verified to be true for all the modes and is not shown here for brevity, a more detailed discussion can be found in Biswas and Buxton (2024*b*). In figure 21, the profiles of $\overline{\tilde{u}^l\tilde{v}^l}$ and $\partial\overline{u}/\partial y$ are shown for the two important wake meandering modes (as shown in figure 17) for the four cases (1, 2c, 3b and 4b) at two streamwise locations, $x/D = 1$ (representative of near wake) and $x/D = 4$ (representative of far wake). Note that, the no grid case shows the strongest gradients in the tip shear layer. However, the wake meandering modes remain sheltered well within the shear layer (see figures 17*a* and 17*b*) in the near wake as well as the far wake, inhibiting it from utilising the stronger gradients available in the shear layer. For the other cases with FST, in the near wake, the wake meandering modes still remain sheltered, explaining the similar wake meandering amplitudes observed for all the cases in the near wake (figure 13). Farther downstream, due to the earlier breakdown of the tip vortices, the modes extend beyond the shear layer (see figure 17). As a result, although the mean velocity gradients are slightly weaker (due to enhanced turbulent mixing), the modes do a better job of exploiting this shear thereby yielding a higher rate of energy transfer from the mean flow.

5.1. *Triadic interactions*

In (5.2), if we only sum over f_t, we can obtain the triadic energy transfer between f_l and f_s. Biswas and Buxton (2024*b*) reported these interfrequency triadic energy transfers in the tip vortex system (formed by the modes $f_r - 6f_r$) for negligible T_i and found the same pattern of triadic energy transfers for a range of λ ($\lambda \geqslant 5.5$). Furthermore, the triadic

https://doi.org/10.1017/jfm.2026.11665 Published online by Cambridge University Press

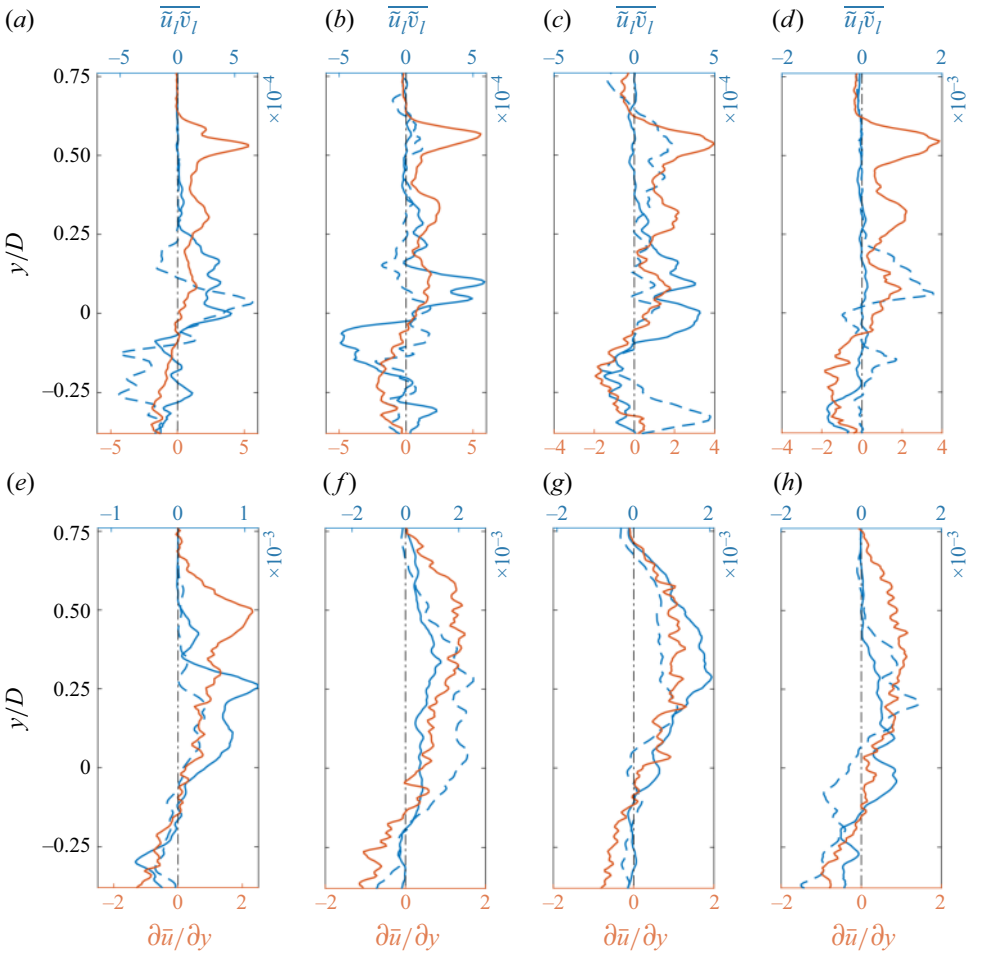


Figure 21. Profiles of coherent velocity correlation ($\overline{\tilde{u}^l\tilde{v}^l}$) and transverse gradient of mean streamwise velocity ($\partial\overline{u}/\partial y$) for the two wake meandering modes (solid and dashed blue lines) extracting the highest amount of energy from the mean flow for the no grid case (*a*,*e*), case 2c (*b*,*f*), case 3b (*c*,*g*) and case 4b (*d*,*h*). The profiles are shown at $x/D = 1$ (*a*–*d*) and $x/D = 4$ (*e*–*h*). The two wake meandering modes are the same as that reported in figure 17.

energy transfers were mainly concentrated within the first four frequencies $f_r - 4f_r$. We perform a similar analysis here for different FST levels. The interfrequency triadic energy transfers (summed over the entire domain) are obtained for select cases (1, 2a, 2c, 3b) and shown in figure 22. Note that no triads were formed for case 4 as f_r and $3f_r$ were the only two frequencies detected in the FOV. For the no grid case, the energy exchange pattern is the same as that observed for $\lambda = 6$ in Biswas and Buxton (2024*b*). Biswas and Buxton (2024*b*) identified two important energy transfer pathways: one from $3f_r$ to f_r via $2f_r$, other from f_r to $3f_r$ via $4f_r$. The former is clearly associated with the tip vortex merging process. The second pathway was considered as a feedback that slowed down the energy drainage of $3f_r$. Interestingly, the same pattern is observed for the low turbulence intensity cases (2a, 2c). However, the transfers were an order of magnitude weaker. It is worthwhile mentioning that for case 2a, the modal decomposition and the energy budget analysis were performed on a truncated domain $x \leqslant 3D$ in order to avoid

https://doi.org/10.1017/jfm.2026.11665 Published online by Cambridge University Press

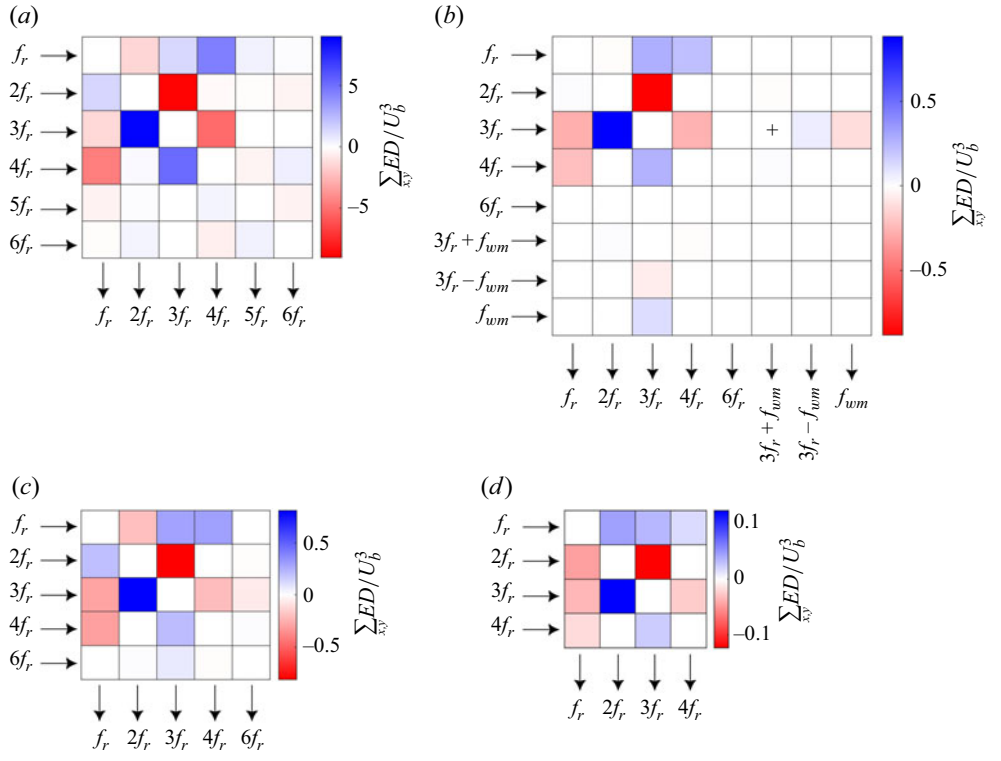


Figure 22. Interfrequency triadic energy transfers for (*a*) no grid case, (*b*) case 2a, (*c*) case 2c and (*d*) case 3b.

boundary layer effects as discussed previously. Nevertheless, it did not impact the values of the total triadic energy fluxes for this case, since the fluxes decayed much before $x = 3D$. From figure 22(*b*) it can be seen that the new frequencies $3f_r \pm f_{wm}$ are energised by $3f_r$, i.e. the mode having the higher frequency among the two main interacting modes. This was not visually clear for $3f_r + f_{wm}$, so a + sign is added in figure 22(*b*). This energy pathway is similar to that observed for the secondary modes in the simple multiscale flow discussed in (Biswas *et al.* 2022). A similar energy exchange pattern is observed for case 3b (figure 22*d*), but the transfer magnitudes were much weaker in comparison with the no grid case. These results quantitatively indicate that FST weakens the tip vortices by weakening the nonlinear triadic energy exchanges, although the fundamental nature of the triadic interactions remain the same.

5.2. *Wake recovery*

The tip vortices in the near wake act as a shield, restricting the exchange of momentum with the freestream (Medici 2005; Lignarolo *et al.* 2015) therefore, it is essential to break them down to initiate the wake recovery process. To understand the link between the tip vortex breakdown process and wake recovery, Biswas and Buxton (2024b) studied the mean flow production term ($\tilde{P}_l$ in (5.1)) of the tip vortex system (consisting of the frequencies $f_r - 6f_r$). It was reported that the tip vortex system exchanges energy with the mean flow primarily through the turbine's rotational frequency f_r. Nearer to the turbine, the f_r mode extracted energy from the mean flow ($\tilde{P}_{f_r} > 0$) and after some distance downstream, it transferred some energy back to the mean flow ($\tilde{P}_{f_r} < 0$) therefore marking the onset location of wake recovery (henceforth denoted by x_w). This sign change in

https://doi.org/10.1017/jfm.2026.11665 Published online by Cambridge University Press

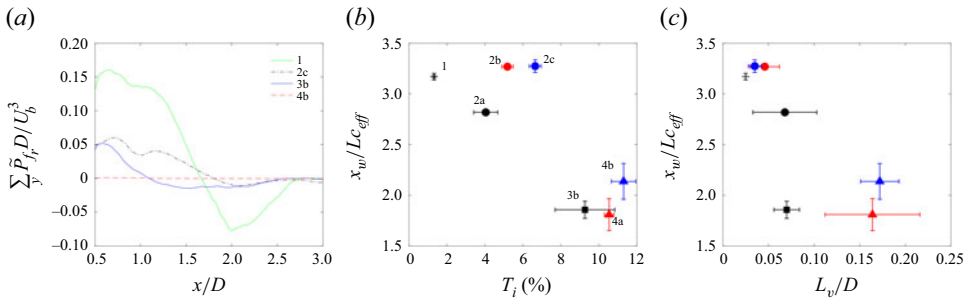


Figure 23. (*a*) Streamwise variation of spanwise averaged mean flow production term for f_r for the different FST cases. The variation of the wake recovery onset location (x_w) is shown against (*b*) T_i and (*c*) L_v. Here x_w is scaled by the convective length scale ($Lc_{eff} = \pi D/\lambda_{eff}$).

$\tilde{P}_{f_r}$ was shown to be due to a change in the inclination of the vortex triplet (having a frequency f_r) produced by merging (Biswas and Buxton 2024*b*). A similar conclusion was reached by Lignarolo *et al.* (2015) for a two bladed turbine.

In figure 23(*a*), we show the streamwise evolution of $\tilde{P}_{f_r}$, summed along y, for four cases of increasing T_i. Note that, a sign change in $\tilde{P}_{f_r}$ is observed even with FST. The streamwise location where it occurs on an average moves upstream as FST intensity is increased. This clearly shows how the wake recovers more quickly in the presence of FST. Figures 23(*b*) and 23(*c*) show how the wake recovery onset location (x_w) changed with T_i and L_v, respectively, for all the cases for which it could be measured. For the cases with the highest T_i, the $\tilde{P}_{f_r}$ term was negligible, at least within the FOV considered, hence, x_w could not be measured. Recently, Biswas and Buxton (2024*a*) introduced a new length scale (termed as the convective pitch, $Lc = \pi D/\lambda$) which could be physically interpreted as the distance travelled by a fluid parcel in the freestream in the time taken by the turbine to complete a single revolution. Note that Lc is not exactly the same as the pitch of the tip vortices as the tip vortices propagate at a velocity slightly smaller than the freestream velocity. In figures 23(*b*) and 23(*c*), x_w is presented in terms of Lc_{eff} which is obtained based on λ_{eff} for each case. Apart from the fact that x_w generally reduces with increasing FST, it appears that for low T_i, x_w scales better with L_v. Although figure 23 lacks data for higher L_v, it is seen that for the highest L_v for which x_w could be calculated, x_w clearly did not follow the decreasing trend observed for lower L_v. This indicates that there is a threshold length scale for which the initiation of wake recovery is the closest to the turbine. Furthermore, this threshold length scale was close to the average size of the tip vortices near the turbine. The size of the tip vortices was calculated by fitting a circle to the phase averaged vorticity field of the tip vortices ($3f_r$) for the no grid case (not shown here). The best fit circle had a diameter $\approx 0.07D$, close to where the trend in figure 23(*c*) changes. This observation is similar to that of Gambuzza & Ganapathisubramani (2023) who noted that for very large integral length scales in a non-Kolmogorov type flow, the near wake length increased back to a value close to the non-turbulent case. Note that the near wake length is loosely connected to the wake recovery location defined here as both depend on the stability of the tip vortices. Another recent study by Bourhis *et al.* (2025) looked at the frequency dynamics in the near wake of a model wind turbine exposed to FST. The smallest integral length scales the authors tested were comparable to the largest studied here. Unsurprisingly, they did not find any clear influence of the integral length scales on the strength of the leading tip vortex frequencies.

https://doi.org/10.1017/jfm.2026.11665 Published online by Cambridge University Press

6. Conclusion

The effect of FST on the multiscale coherent dynamics in a wind turbine wake was studied using PIV measurements. A total of 10 FST cases were studied that had varying turbulence intensity (T_i) and integral length scales (L_v) much smaller than the turbine diameter. The tip vortices were found to break down closer to the turbine in the presence of FST, resulting in an earlier initiation of wake recovery. The onset location of wake recovery (x_w) was found to move closer to the turbine as T_i and L_v were increased. A stronger dependence of x_w on L_v was observed, at least for the low T_i cases considered.

The nature and amplitude of wake meandering at varying FST levels was elucidated. For all the cases, low frequency peaks were observed in the wake that fell in the generally accepted WMFB ($0.15 \leqslant St_D \leqslant 0.4$). In the near wake, the power associated with wake meandering was more comparable for all the cases, showing no clear trend with either T_i or L_v. This indicated that the process of initiation of wake meandering was the same for all the cases, likely related to a turbine instability that is excited by the nacelle's shedding (Howard *et al.* 2015; Foti *et al.* 2016; Biswas and Buxton 2024*a*; Neunaber *et al.* 2025). In the far wake, however, as the wake meandering power for the no grid case (negligible FST) decayed, that for the cases with non-negligible FST levels sustained, primarily due to the earlier breakdown of the tip vortices. For the highest FST cases a broadening of the WMFB was observed (Bourhis *et al.* 2025).

The coherent modes associated with the different frequencies were studied by using OMD. The OMD algorithm identified a larger number of modes in the vicinity of the WMFB that were spatially (and spectrally) similar. These modes were grouped/clustered by using a slightly modified version of the mode clustering algorithm originally introduced by Beit-Sadi *et al.* (2021). The algorithm significantly simplified the OMD spectra, particularly in the vicinity of the WMFB. As the FST level was increased, the tip vortex related modes became weaker and decayed much closer to the turbine. On the other hand, the wake meandering modes for the cases with FST showed a larger spanwise width.

The energy exchanges to/from the modes were studied using the coherent kinetic energy budget equation derived by Baj & Buxton (2017). Even with FST, the wake meandering modes were found to be primarily energised by the mean flow, although there were non-negligible contributions from the diffusion term and triadic interactions. In the presence of FST, the earlier breakdown of the tip vortices allowed the wake meandering modes to better utilise the mean velocity gradient, yielding a higher energy transfer from the mean flow. With FST, the pattern of triadic energy exchanges in the tip vortex system remained almost identical to that reported with negligible FST (Biswas and Buxton 2024*b*). However, the magnitudes of the energy exchanges were drastically reduced for elevated FST levels. New secondary frequencies were reported for the first time that were produced through nonlinear triadic interaction between the tip vortices and wake meandering induced by FST, similarly to our previous studies on multiscale wakes (Baj, & Buxton 2017; Biswas *et al.* 2022).

Our study confirmed that large-scale turbulence ($L_v > D$) is not compulsory to have energetic modes in the meandering frequency band as assumed in the dynamic wake meandering model. When wake meandering is primarily driven by the turbine, even small-scale turbulence can significantly alter wake meandering dynamics, indirectly through breaking down the shield of the tip vortices. This interaction between the tip shear layer and the wake meandering modes after the tip vortices have broken down is not understood properly and deserves future studies. In addition, this work considered the wake only up to a distance of $x = 5D$. Future work should conduct a similar analysis looking at the energy exchanges associated wake meandering farther downstream.

https://doi.org/10.1017/jfm.2026.11665 Published online by Cambridge University Press

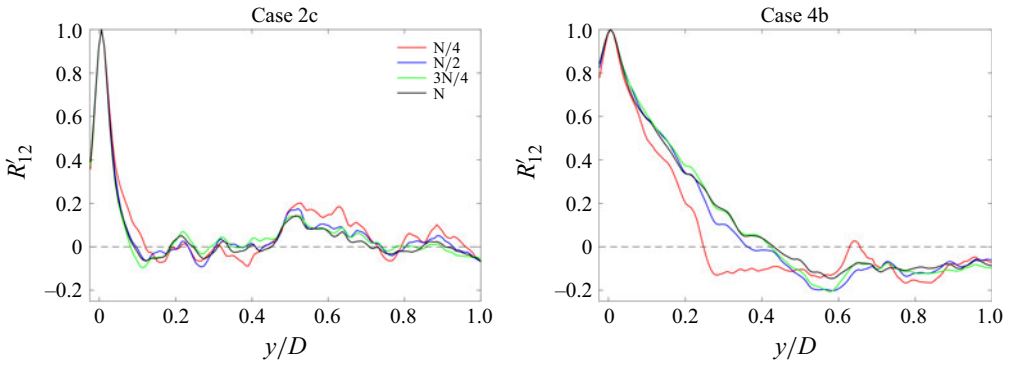


Figure 24. Effect of the data length on the estimation of R'_{12} for the cases 2c and 4b.

A pertinent question to answer would be: Can wake meandering turn into a completely stochastic process farther downstream although its initiation could be related to a turbine instability (having a characteristic frequency)? In the far wake, possible links could be found between wake meandering and meandering observed in other flows (Bailey *et al.* 2018; Bölle 2024).

Supplementary material and movies. Supplementary material and movies are available at https://doi.org/10.1017/jfm.2026.11665.

Funding. N.B. acknowledges support from the Imperial College London President's Scholarship and the Engineering and Physical Sciences Research Council (EPSRC) under grant EP/T51780X/1. O.B. acknowledges support from EPSRC under grant EP/V006436/1.

Declaration of interests. The authors report no conflict of interest.

Appendix A. Uncertainties in the estimation of the integral length scales

Several factors contribute to the uncertainties in the estimation of the integral length scales. Firstly the correlation functions themselves may depend on the length of the time series used. To check this, we evaluated R'_{12} for data truncated in time. Figure 24 here shows the variation of R'_{12} close to the hub height for two different cases, 2c and 4b with different data length (here $N = 5456$ is the total data length in time). Here R'_{12} is found to be generally well converged when the full data is used. The uncertainties in the estimation of the integral length scales were introduced mainly due to the inherent inhomogeneity of the flow cases and due some extent to the use of a fitting function (for cases where it did not fall off to zero). This is further discussed in the Supplementary material.

Appendix B. The OMD-based mode clustering

After identifying the OMD modes, similar modes were identified and clustered. The original mode clustering algorithm proposed by Beit-Sadi *et al.* (2021) is briefly discussed here along with slight changes that have been introduced. For each OMD mode ϕ_l, Beit-Sadi *et al.* (2021) defined a metric $S_l = [\mathrm{Re}(\phi_l), \Im(\phi_l)]$, where Re and $\Im$ denote the real and imaginary parts of ϕ_l and are stored as column vectors. To assess the similarity between modes, the authors used the smallest angle between the subspaces of the modes. The smallest angle between two modes ϕ_l and ϕ_m was therefore measured by using the statistic $\theta_{lm} = \sin^{-1}(||S_l - S_m(S_l^T S_m)||_2)$, where $||.||$ denoted the largest singular value of the matrix. For simplicity, the spatial similarity was then represented by $\zeta = \cos(\theta_{lm})$.

https://doi.org/10.1017/jfm.2026.11665 Published online by Cambridge University Press

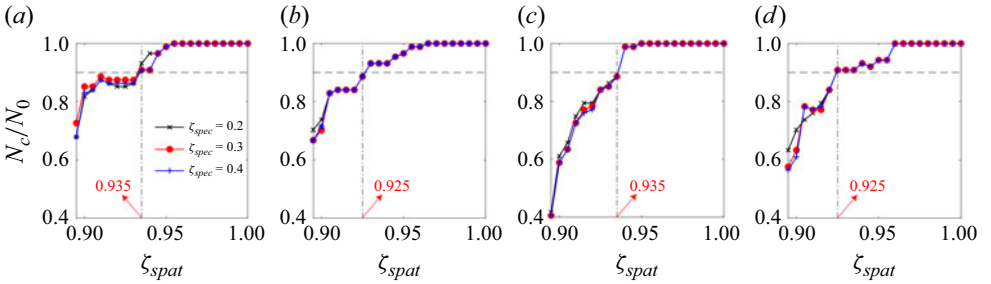


Figure 25. Variation of the number of converged modes (N_c) with ζ_{spat} for different ζ_{spec} for the cases (*a*) 1, (*b*) 2c, (*c*) 3b and (*d*) 4b.

Once the clusters are identified, each of the modes in the cluster are stacked in a matrix (let us denote it as M) as column vectors multiplied by a significance parameter or weight σ_l. If the kth cluster has n modes, then $M_k = [\sigma_1\phi_1, \sigma_2\phi_2 \ldots \sigma_n\phi_n]$. Thereafter, a singular value decomposition of M_k is performed and the first singular vector is used as the mode representing the cluster. However, it is worthwhile to note that several aspects of the method are still not strictly defined and deserve further consideration. One of them is how to assign a frequency and growth rate to a clustered mode. Further, which statistic is the best to use as σ? For example, one could project the snapshots on the OMD modes to obtain the time varying coefficients of the modes. The magnitude of the coefficient at a specific time or a norm of the coefficient could be used as σ. Here, however, it was found that using such a statistic undermined the influence of the lesser damped modes within a cluster. Accordingly, a quantity related to the growth rate ($\mathrm{Re}(\gamma_{OMD})$) of the modes was thought to be a more reasonable measure of σ motivating the use of the quantity $1/|\mathrm{Re}(\gamma_{OMD})|$. The dominant modes (growth rate closer to zero) are therefore assigned a higher significance value. This method showed faster convergence for the current data set and yielded better converged modes representing a cluster. The modes representing a cluster are also assigned a virtual growth rate and a frequency which is obtained by taking a weighted average of the frequencies and growth rates of the modes forming a cluster with σ used as the weight. The whole process is repeated until no two modes are similar.

The choice of the spatial and spectral similarity cutoffs ζ_{spat} and ζ_{spec} also involves some subjectivity. The effects of ζ_{spat} and ζ_{spec} on the converged number of modes (N_c) for the four main cases are shown in figure 25. The rank of OMD was set to 175 (i.e. the total number of initial modes $N_0 = 175$) for all cases following our previous work (Biswas and Buxton 2024*b*). No mode reduction is achieved for $\zeta_{spat} \geqslant 0.96$, while for $\zeta_{spat} \leqslant 0.9$ the spectra are over simplified leaving too few modes. A different ζ_{spat} was selected for each case such that $N_c/N_0 \approx 0.9$ could be achieved. For the cases shown in figure 25, the selected cutoffs are shown by the vertical dashed line. The different symbols in figure 25 correspond to different values of ζ_{spec}. Note that the mode clustering process does not depend significantly on ζ_{spec} for $\zeta_{spec} \geqslant 0.2$. The analysis was therefore continued with $\zeta_{spec} = 0.3$ for all the cases.

Appendix C. Mode selection and reduced-order representation of the flow

Although mode clustering simplifies the OMD spectrum, care must be taken while selecting modes from the reduced spectrum (after performing mode clustering) to represent the coherent component of the flow. The lesser damped modes generally represent a physically meaningful mode, but drawing a cutoff on the growth rate

https://doi.org/10.1017/jfm.2026.11665 Published online by Cambridge University Press

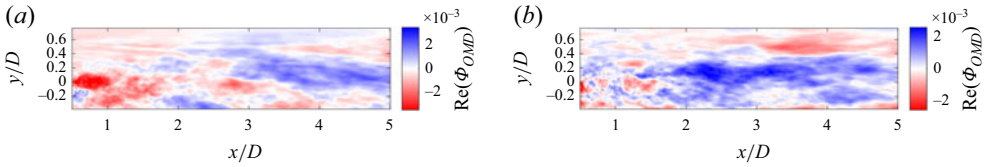


Figure 26. Example low frequency modes for the (*a*) no grid case and (*b*) case 4b that are not considered to be a part of the coherent component of the flow and are likely attributable to an intermittent large-scale phenomenon. The real part of the OMD modes (Re(ϕ_{OMD})) is shown.

(Re(γ_{OMD})) is subjective. Looking at the nature of the spectra, the modes with Re(γ_{OMD}) $\gtrsim -0.05$, or in that vicinity, were considered. Before selecting a mode, each mode shape had to be checked manually to see if they show any physically meaningful structure. Sometimes a slightly more damped mode had to be selected since its spatial coherence was more interpretable in a physically meaningful way. Occasionally some modes were not selected despite being less damped than some other selected modes (example figure 16*c*). The spatial shape of these modes revealed very large-scale smeared structures which were likely due to the intermittent passage of large-scale structures having a size smaller than that indicated by the mode shapes. Example of such modes are shown in figure 26 for the no grid case and case 4b. These modes are also highlighted by a blue arrow in the spectra shown in figures 16(*c*) and 16(*l*). Furthermore, when a mode was obtained by clustering other modes, the growth rate of the new mode was simply calculated as a weighted average of the growth rates of the modes forming the cluster. This was done simply to place the new mode somewhere in the spectrum and this growth rate need not have any physical meaning. In summary, the shape of the modes involved in clustering was always checked irrespective of their growth rates.

References

Abraham, A., Dasari, T. & Hong, J. 2019 Effect of turbine nacelle and tower on the near wake of a utility-scale wind turbine. *J. Wind Engng Ind. Aerod.* **193**, 103981.

Abraham, A. & Leweke, T. 2023 Experimental investigation of blade tip vortex behavior in the wake of asymmetric rotors. *Exp. Fluids* **64** (6), 109.

Andersen, S.J., Sørensen, J.N. & Mikkelsen, R. 2013 Simulation of the inherent turbulence and wake interaction inside an infinitely long row of wind turbines. *J. Turbul.* **14** (4), 1–24.

Ashton, R., Viola, F., Camarri, S., Gallaire, F., Iungo, G.V., *et al.* 2016 Hub vortex instability within wind turbine wakes: effects of wind turbulence, loading conditions, and blade aerodynamics. *Phys. Rev. Fluids* **1**, 1–18.

Bailey, S.C., Pentelow, S., Ghimire, H.C., Estejab, B., Green, M.A. & Tavoularis, S. 2018 Experimental investigation of the scaling of vortex wandering in turbulent surroundings. *J. Fluid Mech.* **843**, 722–747.

Baj, P., Bruce, P.J.K. & Buxton, O.R.H. 2015 The triple decomposition of a fluctuating velocity field in a multiscale flow. *Phys. Fluids* **27** (7), 075104.

Baj, P. & Buxton, O.R.H. 2017 Interscale energy transfer in the merger of wakes of a multiscale array of rectangular cylinders. *Phys. Rev. Fluids* **2** (11), 114607.

Barlas, E., Buckingham, S. & van Beeck, J. 2016 Roughness effects on wind-turbine wake dynamics in a boundary-layer wind tunnel. *Boundary-Layer Meteorol.* **158**, 27–42.

Barthelmie, R.J., Frandsen, S.T., Nielsen, M., Pryor, S., Rethore, P.-E. & Jørgensen, H.E. 2007 Modelling and measurements of power losses and turbulence intensity in wind turbine wakes at middelgrunden offshore wind farm. *Wind Energy: Intl J. Progress Appl. Wind Power Convers. Technol.* **10** (6), 517–528.

Barthelmie, R., Hansen, O.F., Enevoldsen, K., Højstrup, J., Frandsen, S., Pryor, S., Larsen, S., Motta, M. & Sanderhoff, P. 2005 Ten years of meteorological measurements for offshore wind farms. *J. Sol. Energy Engng* **127** (2), 170–176.

https://doi.org/10.1017/jfm.2026.11665 Published online by Cambridge University Press

BEARMAN, P. & MOREL, T. 1983 Effect of free stream turbulence on the flow around bluff bodies. *Prog. Aerosp. Sci.* **20** (2–3), 97–123.
BEIT-SADI, M., KROL, J. & WYNN, A. 2021 Data-driven feature identification and sparse representation of turbulent flows. *Intl J. Heat Fluid Flow* **88**, 108766.
BISWAS, N. & BUXTON, O.R. 2024*a* Effect of tip speed ratio on coherent dynamics in the near wake of a model wind turbine. *J. Fluid Mech.* **979** , A34.
BISWAS, N. & BUXTON, O.R. 2024*b* Energy exchanges between coherent modes in the near wake of a wind turbine model at different tip speed ratios. *J. Fluid Mech.* **996** , A8.
BISWAS, N., CICOLIN, M.M. & BUXTON, O.R.H. 2022 Energy exchanges in the flow past a cylinder with a leeward control rod. *J. Fluid Mech.* **941**, A36.
BLACKMORE, T., BATTEN, W. & BAHAJ, A. 2014 Influence of turbulence on the wake of a marine current turbine simulator. *Proc. R. Soc. A: Math. Phys. Engng Sci.* **470** (2170), 20140331.
BLACKMORE, T., MYERS, L.E. & BAHAJ, A.S. 2016 Effects of turbulence on tidal turbines: implications to performance, blade loads, and condition monitoring. *Intl J. Mar. Energy* **14**, 1–26.
BOURHIS, M., MESSMER, T., HÖLLING, M. & BUXTON, O. 2025 Impact of free-stream turbulence and thrust coefficient on wind turbine-generated wakes. *J. Fluid Mech.* **1023**, A3.
BÖLLE, T. 2024 On the linear response theory of vortex meandering and its statistical verification in experiments. *J. Fluid Mech.* **997**, A38.
CHAMORRO, L., GUALA, M., ARNDT, R. & SOTIROPOULOS, F. 2012 On the evolution of turbulent scales in the wake of a wind turbine model. *J. Turbul.* **13**, N27.
CHAMORRO, L., HILL, C., MORTON, S., ELLIS, C., ARNDT, R. & SOTIROPOULOS, F. 2013 On the interaction between a turbulent open channel flow and an axial-flow turbine. *J. Fluid Mech.* **716**, 658.
CHAMORRO, L.P. & PORTÉ-AGEL, F. 2009 A wind-tunnel investigation of wind-turbine wakes: boundary-layer turbulence effects. *Boundary-Layer Meteorol.* **132** (1), 129–149.
CHEN, J. & BUXTON, O.R. 2023 Spatial evolution of the turbulent/turbulent interface geometry in a cylinder wake. *J. Fluid Mech.* **969**, A4.
CICOLIN, M., BUXTON, O., ASSI, G. & BEARMAN, P. 2021 The role of separation on the forces acting on a circular cylinder with a control rod. *J. Fluid Mech.* **915**, A33.
DE CILLIS, G., CHERUBINI, S., SEMERARO, O., LEONARDI, S. & DE PALMA, P. 2021 POD-based analysis of a wind turbine wake under the influence of tower and nacelle. *Wind Energy* **24** (6), 609–633.
DEBNATH, M., SANTONI, C., LEONARDI, S. & IUNGO, G.V. 2017 Towards reduced order modelling for predicting the dynamics of coherent vorticity structures within wind turbine wakes. *Phil. Trans. R. Soc. A: Math. Phys. Engng Sci.* **375** (2091), 20160108.
DESMOND, C., MURPHY, J., BLONK, L. & HAANS, W. 2016 Description of an 8 mw reference wind turbine. *J. Phys.: Conf. Ser.* **753**, 092013.
DONG, G., QIN, J., LI, Z. & YANG, X. 2023 Characteristics of wind turbine wakes for different blade designs. *J. Fluid Mech.* **965**, A15.
EGGERS, A., Jr, DIGUMARTHI, R. & CHANEY, K. 2003 Wind shear and turbulence effects on rotor fatigue and loads control. *J. Sol. Energy Engng* **125** (4), 402–409.
ELLIOTT, D.L. & CADOGAN, J.B. 1990 Effects of wind shear and turbulence on wind turbine power curves. *Tech. Rep.* PNL-SA-18354; CONF-900989–2; ON: DE91004072. Pacific Northwest Lab.
ERIKSEN, P.E. & KROGSTAD, P.-Å. 2017 Development of coherent motion in the wake of a model wind turbine. *Renew. Energy* **108**, 449–460.
ESPANA, G., AUBRUN, S., LOYER, S. & DEVINANT, P. 2011 Spatial study of the wake meandering using modelled wind turbines in a wind tunnel. *Wind Energy* **14** (7), 923–937.
ESPANA, G., AUBRUN, S., LOYER, S. & DEVINANT, P. 2012 Wind tunnel study of the wake meandering downstream of a modelled wind turbine as an effect of large scale turbulent eddies. *J. Wind Engng Ind. Aerodyn.* **101**, 24–33.
FOTI, D., YANG, X., GUALA, M. & SOTIROPOULOS, F. 2016 Wake meandering statistics of a model wind turbine: insights gained by large eddy simulations. *Phys. Rev. Fluids* **1** (4), 044407.
FOTI, D., YANG, X. & SOTIROPOULOS, F. 2018 Similarity of wake meandering for different wind turbine designs for different scales. *J. Fluid Mech.* **842**, 5.
FRANSSON, J.H., MATSUBARA, M. & ALFREDSSON, P.H. 2005 Transition induced by free-stream turbulence. *J. Fluid Mech.* **527**, 1–25.
FUERTES, F.C., MARKFORT, C.D. & PORTÉ-AGEL, F. 2018 Wind turbine wake characterization with nacelle-mounted wind lidars for analytical wake model validation. *Remote Sens.-Basel* **10** (5), 668.
GAMBUZZA, S. & GANAPATHISUBRAMANI, B. 2023 The influence of free stream turbulence on the development of a wind turbine wake. *J. Fluid Mech.* **963**, A19.

https://doi.org/10.1017/jfm.2026.11665 Published online by Cambridge University Press

GUPTA, V. & WAN, M. 2019 Low-order modelling of wake meandering behind turbines. *J. Fluid Mech.* **877**, 534–560.
HEARST, R.J., DOGAN, E. & GANAPATHISUBRAMANI, B. 2018 Robust features of a turbulent boundary layer subjected to high-intensity free-stream turbulence. *J. Fluid Mech.* **851**, 416–435.
HEARST, R.J. & LAVOIE, P. 2015 The effect of active grid initial conditions on high Reynolds number turbulence. *Exp. Fluids* **56** (10), 185.
HEISEL, M., HONG, J. & GUALA, M. 2018 The spectral signature of wind turbine wake meandering: a wind tunnel and field-scale study. *Wind Energy* **21** (9), 715–731.
HODGSON, E.L., MADSEN, M.H.A. & ANDERSEN, S.J. 2023 Effects of turbulent inflow time scales on wind turbine wake behavior and recovery. *Phys. Fluids* **35** (9), 095125.
HOWARD, K.B., SINGH, A., SOTIROPOULOS, F. & GUALA, M. 2015 On the statistics of wind turbine wake meandering: an experimental investigation. *Phys. Fluids* **27** (7), 075103.
IUNGO, G.V., VIOLA, F., CAMARRI, S., PORTÉ-AGEL, F. & GALLAIRE, F. 2013 Linear stability analysis of wind turbine wakes performed on wind tunnel measurements. *J. Fluid Mech.* **737**, 499–526.
JIN, Y., LIU, H., AGGARWAL, R., SINGH, A. & CHAMORRO, L.P. 2016 Effects of freestream turbulence in a model wind turbine wake. *Energies* **9** (10), 830.
KANKANWADI, K.S. & BUXTON, O.R. 2020 Turbulent entrainment into a cylinder wake from a turbulent background. *J. Fluid Mech.* **905**, A35.
KINJANGI, D.K. & FOTI, D. 2023 Characterization of energy transfer and triadic interactions of coherent structures in turbulent wakes. *J. Fluid Mech.* **971**, A7.
KOSOVIĆ, B., BASU, S., BERG, J., BERG, L.K., HAUPT, S.E., LARSÉN, X.G., PEINKE, J., STEVENS, R.J., VEERS, P. & WATSON, S. 2025 Impact of atmospheric turbulence on performance and loads of wind turbines: knowledge gaps and research challenges. *Wind Energy Sci. Discuss.* **2025**, 1–67.
KURIAN, T. & FRANSSON, J.H. 2009 Grid-generated turbulence revisited. *Fluid Dyn. Res.* **41** (2), 021403.
LARSEN, G.C., *et al.* 2007 *Dynamic Wake Meandering Modeling*. Risø National Laboratory.
LARSEN, G.C., MADSEN, H.A., THOMSEN, K. & LARSEN, T.J. 2008 Wake meandering: a pragmatic approach. *Wind Energy: Intl J. Prog. Appl. Wind Power Convers. Technol.* **11** (4), 377–395.
LIGNAROLO, L., RAGNI, D., SCARANO, F., FERREIRA, C.S. & VAN BUSSEL, G. 2015 Tip-vortex instability and turbulent mixing in wind-turbine wakes. *J. Fluid Mech.* **781**, 467.
MAGANGA, F., GERMAIN, G., KING, J., PINON, G. & RIVOALEN, E. 2010 Experimental characterisation of flow effects on marine current turbine behaviour and on its wake properties. *IET Renew. Power Gener.* **4** (6), 498–509.
MAO, X. & SØRENSEN, J. 2018 Far-wake meandering induced by atmospheric eddies in flow past a wind turbine. *J. Fluid Mech.* **846**, 190–209.
MARYAMI, R., ALI, S.A.S., AZARPEYVAND, M. & AFSHARI, A. 2020 Turbulent flow interaction with a circular cylinder. *Phys. Fluids* **32** (1), 015105.
MAZELLIER, N. & VASSILICOS, J.C. 2010 Turbulence without Richardson–Kolmogorov cascade. *Phys. Fluids* **22** (7), 075101.
MEDICI, D. 2005 Experimental studies of wind turbine wakes: power optimisation and meandering. PhD thesis, KTH.
MEDICI, D. & ALFREDSSON, P.H. 2008 Measurements behind model wind turbines: further evidence of wake meandering. *Wind Energy: Intl J. Prog. Appl. Wind Power Convers. Technol.* **11** (2), 211–217.
MILLER, M.A., KIEFER, J., WESTERGAARD, C., HANSEN, M.O. & HULTMARK, M. 2019 Horizontal axis wind turbine testing at high Reynolds numbers. *Phys. Rev. Fluids* **4** (11), 110504.
NEUNABER, I., HÖLLING, M., STEVENS, R.J., SCHEPERS, G. & PEINKE, J. 2020 Distinct turbulent regions in the wake of a wind turbine and their inflow-dependent locations: the creation of a wake map. *Energies* **13** (20), 5392.
NEUNABER, I., YADALA, S. & HEARST, R.J. 2025 Induced periodicity in wakes. *J. Fluid Mech.* **1022**, R3.
NIAYIFAR, A. & PORTÉ-AGEL, F. 2016 Analytical modeling of wind farms: a new approach for power prediction. *Energies* **9** (9), 741.
NORBERG, C. 1986 Interaction between freestream turbulence and vortex shedding for a single tube in cross-flow. *J. Wind Engng Ind. Aerod.* **23**, 501–514.
OKULOV, V., NAUMOV, I., MIKKELSEN, R., KABARDIN, I. & SØRENSEN, J. 2014 A regular Strouhal number for large-scale instability in the far wake of a rotor. *J. Fluid Mech.* **747**, 369.
DE OLIVEIRA, F.J., KHODAEI, Z.S. & BUXTON, O.R. 2025 The influence of free-stream turbulence on the fluctuating loads experienced by a cylinder exposed to a turbulent cross-flow. *J. Fluid Mech.* **1011**, A47.
PEÑA, A., FLOORS, R., SATHE, A., GRYNING, S.-E., WAGNER, R., COURTNEY, M.S., LARSÉN, X.G., HAHMANN, A.N. & HASAGER, C.B. 2016 Ten years of boundary-layer and wind-power meteorology at Høvsøre, Denmark. *Boundary-Layer Meteorol.* **158**, 1–26.

https://doi.org/10.1017/jfm.2026.11665 Published online by Cambridge University Press

PORTÉ-AGEL, F., BASTANKHAH, M. & SHAMSODDIN, S. 2020 Wind-turbine and wind-farm flows: a review. *Boundary-Layer Meteorol.* **174** (1), 1–59.

RIND, E. & CASTRO, I.P. 2012 On the effects of free-stream turbulence on axisymmetric disc wakes. *Exp. Fluids* **53** (2), 301–318.

ROBERTSON, A.N., SHALER, K., SETHURAMAN, L. & JONKMAN, J. 2019 Sensitivity analysis of the effect of wind characteristics and turbine properties on wind turbine loads. *Wind Energy Sci.* **4** (3), 479–513.

SANDERSE, B., VAN DER PIJL, S. & KOREN, B. 2011 Review of computational fluid dynamics for wind turbine wake aerodynamics. *Wind Energy* **14** (7), 799–819.

SARMAST, S., DADFAR, R., MIKKELSEN, R.F., SCHLATTER, P., IVANELL, S., SØRENSEN, J.N. & HENNINGSON, D.S. 2014 Mutual inductance instability of the tip vortices behind a wind turbine. *J. Fluid Mech.* **755**, 705–731.

SCHMID, P.J. 2010 Dynamic mode decomposition of numerical and experimental data. *J. Fluid Mech.* **656**, 5–28.

SHERRY, M., NEMES, A., JACONO, D.L., BLACKBURN, H.M. & SHERIDAN, J. 2013 The interaction of helical tip and root vortices in a wind turbine wake. *Phys. Fluids* **25** (11), 117102.

SINGH, A., HOWARD, K.B. & GUALA, M. 2014 On the homogenization of turbulent flow structures in the wake of a model wind turbine. *Phys. Fluids* **26** (2), 025103.

SIROVICH, L. 1987 Turbulence and the dynamics of coherent structures, parts I, II and III. *Q. Appl. Math.* 561–590.

STANISLAWSKI, B.J., THEDIN, R., SHARMA, A., BRANLARD, E., VIJAYAKUMAR, G. & SPRAGUE, M.A. 2023 Effect of the integral length scales of turbulent inflows on wind turbine loads. *Renew. Energy* **217**, 119218.

STEVENS, R.J. & MENEVEAU, C. 2017 Flow structure and turbulence in wind farms. *Annu. Rev. Fluid Mech.* **49**, 311–339.

TÜRK, M. & EMEIS, S. 2010 The dependence of offshore turbulence intensity on wind speed. *J. Wind Engng Ind. Aerodyn.* **98** (8–9), 466–471.

VAHIDI, D. & PORTÉ-AGEL, F. 2024 Influence of incoming turbulent scales on the wind turbine wake: a large-eddy simulation study. *Phys. Fluids* **36** (9), 095177.

VERMEER, L., SØRENSEN, J.N. & CRESPO, A. 2003 Wind turbine wake aerodynamics. *Prog. Aerosp. Sci.* **39** (6–7), 467–510.

VIOLA, F., IUNGO, G.V., CAMARRI, S., PORTÉ-AGEL, F. & GALLAIRE, F. 2014 Prediction of the hub vortex instability in a wind turbine wake: stability analysis with eddy-viscosity models calibrated on wind tunnel data. *J. Fluid Mech.* **750**, R1.

WAGNER, R., COURTNEY, M., GOTTSCHALL, J. & LINDELÖW-MARSDEN, P. 2011 Accounting for the speed shear in wind turbine power performance measurement. *Wind Energy* **14** (8), 993–1004.

WANG, Y., ZHAO, G., LIU, G., ZHOU, Y., GE, M., OUYANG, Z., DING, Z. & HU, R. 2025 Effects of tip speed ratio on wind turbine wake meandering. *J. Fluid Mech.* **1014**, A3.

WELCH, P. 1967 The use of fast fourier transform for the estimation of power spectra: a method based on time averaging over short, modified periodograms. *IEEE Trans. Acoust. Speech* **15** (2), 70–73.

WU, Y.-T. & PORTÉ-AGEL, F. 2012 Atmospheric turbulence effects on wind-turbine wakes: an LES study. *Energies* **5** (12), 5340–5362.

WYNN, A., PEARSON, D., GANAPATHISUBRAMANI, B. & GOULART, P.J. 2013 Optimal mode decomposition for unsteady flows. *J. Fluid Mech.* **733**, 473–503.

YEUNG, B., CHU, T. & SCHMIDT, O.T. 2024 Revealing structure and symmetry of nonlinearity in natural and engineering flows. arXiv preprint arXiv:2411.12057.

https://doi.org/10.1017/jfm.2026.11665 Published online by Cambridge University Press